# Oncogene-induced senescence mitochondrial metabolism and bioenergetics drive the secretory phenotype: further characterization and comparison with other senescence-inducing stimuli

Inés Marmisolle [a,b], Eliana Chacón [a,b], Santiago Mansilla [b,c], Santiago Ruiz [d], Mariana Bresque [d], Jennyfer Martínez [a,b], Ricardo Iván Martínez-Zamudio [e], Utz Herbig [f], Jie Liu [g], Toren Finkel [g], Carlos Escande [d], Laura Castro [a,b], Celia Quijano [a,b,*]

[a] *Departamento de Bioquímica, Facultad de Medicina, Universidad de la República, Uruguay*
[b] *Centro de Investigaciones Biomédicas (CEINBIO), Universidad de la República, Uruguay*
[c] *Departamento de Métodos Cuantitativos, Facultad de Medicina, Universidad de la República, Uruguay*
[d] *Laboratorio de Patologías del Metabolismo y el Envejecimiento, Institut Pasteur de Montevideo, Uruguay*
[e] *Department of Pharmacology, Robert Wood Johnson Medical School, Rutgers University, Piscataway, NJ, 08854, USA*
[f] *Center for Cell Signaling, Department of Microbiology, Biochemistry, and Molecular Genetics, New Jersey Medical School, Rutgers University, Newark, NJ, 07103, USA*
[g] *Aging Institute, University of Pittsburgh School of Medicine, Pittsburgh, PA, USA*

## ARTICLE INFO

## ABSTRACT

Cellular senescence is characterized by proliferation arrest and a senescence-associated secretory phenotype (SASP), that plays a role in aging and the progression of various age-related diseases. Although various metabolic alterations have been reported, no consensus exists regarding mitochondrial bioenergetics. Here we compared mitochondrial metabolism of human fibroblasts after inducing senescence with different stimuli: the oxidant hydrogen peroxide ($H_2O_2$), the genotoxic doxorubicin, serial passage, or expression of the H-RAS$^{G12V}$ oncogene (RAS).

In senescence induced by $H_2O_2$, doxorubicin or serial passage a decrease in respiratory control ratio (RCR) and coupling efficiency was noted, in relation to control cells. On the contrary, oncogene-induced senescent cells had an overall increase in respiration rates, RCR, spare respiratory capacity and coupling efficiency. In oncogene-induced senescence (OIS) the increase in respiration rates was accompanied by an increase in fatty acid catabolism, AMPK activation, and a persistent DNA damage response (DDR), that were not present in senescent cells induced by either $H_2O_2$ or doxorubicin. Inhibition of AMPK reduced mitochondrial oxygen consumption and secretion of proinflammatory cytokines in OIS.

Assessment of enzymes involved in acetyl-CoA metabolism in OIS showed a 3- to 7.5-fold increase in pyruvate dehydrogenase complex (PDH), a 40% inhibition of mitochondrial aconitase, increased phosphorylation and activation of ATP-citrate lyase (ACLY), and inhibition of acetyl-CoA carboxylase (ACC). There was also a significant increase in expression and nuclear levels of the deacetylase sirtuin 6 (SIRT6). These changes can influence the sub-cellular distribution of acetyl-CoA and modulate protein acetylation reactions in the cytoplasm and nuclei. In fact, ACLY inhibition reduced histone 3 acetylation (H3K9Ac) in OIS and secretion of SASP components.

In summary, our data show marked heterogeneity in mitochondrial energy metabolism of senescent cells, depending on the inducing stimulus, reveal new metabolic features of oncogene-induced senescent cells and identify AMPK and ACLY as potential targets for SASP modulation.

---

**Abbreviations**

| | |
|---|---|
| AA | antimycin A |
| ACC | acetyl-CoA carboxylase |
| ACLY | ATP-citrate-lyase |
| AcLys | lysine acetylation |
| AMPK | AMP-activated protein kinase |
| ACO2 | mitocondrial aconitase |
| ATM | ataxia-telangiectasia mutated kinase |
| BAY | BAY 11-7082 |
| BSA | bovine serum albumin |
| CC | compound C/dorsomorphin |
| CM-H$_2$DCFDA | chloromethyl-2′,7′-dichlorodihydrofluorescein diacetate |
| CM- H$_2$DCF | chloromethyl-2′,7′-dichlorodihydrofluorescein |
| CM-DCF | chloromethyl-2′,7′-dichlorofluorescein |
| CPT1 | carnitine palmitoyltransferase 1 |
| DDR | DNA damage response |
| DMSO | dimethylsulfoxide |
| Doxo | doxorubicin |
| ERK1/2 | extracellular signal-regulated kinases 1/2 |
| Eto | etomoxir |
| FCCP | 4-(trifluoromethoxy)phenylhydrazone |
| H$_2$O$_2$ | hydrogen peroxide |
| IκB | NF-κB inhibitor |
| IKK | IκB kinase |
| IL-6 | interleukin-6 |
| IL-8 | interleukin-8 |
| MAPK | mitogen activated protein kinase |
| MAVS | mitochondrial antiviral-signaling proteins |
| NDI | NDI-091143 |
| NFκB | nuclear factor-κB |
| OA | oleic acid |
| OCR | oxygen consumption rate |
| 4OHT | 4-hydroxytamoxifen |
| OIS | oncogene-induced senescence |
| Oligo | oligomycin |
| O$_2^{\cdot-}$ | superoxide |
| PDH | pyruvate dehydrogenase complex |
| p16-INK4 or CDKN2A | cyclin-dependent kinase inhibitor 2A |
| p21 or CDKN1A | cyclin-dependent kinase inhibitor 1 |
| RAS | H-RAS$^{G12V}$ oncogene |
| RCR | respiratory control ratio |
| RS | replicative senescence |
| SASP | senescence-associated secretory phenotype |
| SA-β-Gal | senescence-associated β-galactosidase activity |
| SIRT1 | sirtuin 1 |
| SIRT3 | sirtuin 3 |
| SIRT6 | sirtuin 6 |
| SIS | stress-induced senescence |
| TCA | Tricarboxylic acid |
| WB | western blots |

## 1. Introduction

Cellular senescence is a state triggered by different stressful stimuli, as well as some physiological conditions. Among the features of senescent cells, is a proliferation arrest mediated persistent hypophosphorylation of the retinoblastoma protein (pRb), usually mediated by cyclin-dependent kinase inhibitor 2A (CDKN2A, p16-INK4)[1] and/or cyclin-dependent kinase inhibitor 1 (CDNK1A, p21). Senescent cells also experience nuclear changes, such as a decrease in lamin B1 and post-translational modifications of histones and DNA methylation [1,2]. Other characteristics shared by senescent cells are the increase in macromolecular damage, for example in DNA, that is usually accompanied by activation of the DNA damage response (DDR) and the acquisition of a senescence-associated secretory phenotype (SASP) [1, 2]. Senescent cells are also resistant to apoptosis [3] and usually present important changes in size and morphology, as well as in organelle content [4]. In fact, the increase in senescence-associated β-galactosidase activity (SA-β-Gal), due to an expansion of the lysosomal compartment, is one of the most extensively used markers for this state [5]. However, heterogeneity can be found, depending on the cell type and the stimuli that induced the senescent phenotype, as well as the time point after induction [6]. Alterations in metabolism have also been observed in senescent cells, and mitochondria in particular have been the focus of several studies [7–17].

Mitochondria, constitute the main energy-producing center of most eukaryotic cells. However, their role goes beyond ATP synthesis, including modulating apoptosis, calcium storage, and reactive oxygen species formation [18]. In addition, mitochondria constitute structural platforms for the assembly of complexes such as the inflammasome and mitochondrial antiviral signaling proteins (MAVS), and participate in signal transduction [19–22]. In particular, mitochondrial oxidant species, mtDNA and mtRNA appear to play relevant roles in the establishment of senescence and the SASP [23][16,24].

Mitochondria house several catabolic, oxidative pathways for the conversion of nutrients to simpler metabolites. In the mitochondrial matrix, fatty acids and pyruvate are degraded to acetyl-CoA in the β-oxidation pathway and the pyruvate dehydrogenase complex (PDH), respectively, and ATP is synthesized by oxidative phosphorylation [25].

Due to the diversity of roles played by mitochondria the term "mitochondrial dysfunction" has been applied to account for different alterations, and can sometimes be misleading [18]. For example, several authors report mitochondrial dysfunction in senescence, having observed increases in AMP-activated protein kinase (AMPK), mitochondrial reactive species and lower mitochondrial membrane potential [9,11]. However, in oncogene-induced senescence (OIS) and therapy-induced senescence (TIS) an increase in mitochondrial catabolism has been shown, including the electron transport chain, PDH, β-oxidation and NAD$^+$ salvage pathway [12–15,26–28]. High oxygen consumption rates were also observed in replicative senescence [26,29]. Mitochondrial biogenesis and consequently mitochondrial mass and mtDNA copy number are also higher in OIS, TIS, replicative and DNA-damage induced senescence when compared to control cells [9–11, 14]. Interestingly, high glucose uptake and lactic fermentation were also noted in senescent cells, suggesting an overall increase in energy metabolism [15,17,26,27,29,30].

Mitochondrial depletion, specific inhibition of fatty acid mitochondrial oxidation, NAD$^+$ biosynthesis or mitochondrial electron transport, impair the secretion of proinflammatory factors by senescent cells [10, 13,27,31], underscoring the relevance of mitochondrial energy metabolism for the establishment of the SASP.

To better understand mitochondrial energy metabolism in senescent cells, we compared the oxygen consumption rates of human lung fibroblasts after inducing senescence with different stimuli: stress-induced senescence (SIS) by exposure to the oxidant hydrogen peroxide (H$_2$O$_2$) or the genotoxic doxorubicin; OIS by expression of the H-RAS$^{G12V}$ oncogene (RAS); or replicative senescence (RS) induced by serial passage. Our results reveal heterogeneity in mitochondrial energy metabolism of senescent cells, depending on the inducing stimulus. Besides, we explored metabolic pathways and their regulation in RAS-induced senescent cells, observing an increase in catabolic routes that responds to energy demands, and channels acetyl moieties to the cytosol facilitating ATP-citrate lyase (ACLY) mediated histone acetylation and

the SASP. Finally, we established that activation of AMPK, master regulator of energy metabolism, is required for the increase in respiration rates and cytokine secretion in OIS.

## 2. Results

### 2.1. Mitochondrial fatty acid oxidation in senescent fibroblasts induced with different stimuli

Previous work from our group showed a decrease in fatty acid synthesis in senescent cells induced by RAS oncogene expression [13], telomere attrition (RS) or exposure to the DNA damaging agents $H_2O_2$ or doxorubicin [32]. In these settings, changes were observed in acetyl-CoA carboxylase (ACC) an enzyme that catalyzes the synthesis of malonyl-CoA, a relevant intermediate in fatty acid synthesis, and

regulator of fatty acid entrance into mitochondria. These results prompted us to compare fatty acid oxidation in these different models of senescence in human lung fibroblasts (IMR-90).

We exposed the cells to $H_2O_2$ or doxorubicin, or transduced them with lentiviral particles carrying H-RAS[G12V]. Experiments were performed 14 days after exposure to the senescence inducing stimuli, when 60% or more of the cells in the treated culture were positive for SA-β-Gal (Fig. 1A–C). Hypophosphorylation of the retinoblastoma protein (pRb) and inhibition of culture growth were observed in all cases, along with a decrease in *LMNB1* (lamin B1) expression (Supplementary Fig. S1) and morphological changes, such as an increase in size (Fig. 1A–C). Nevertheless differences were found between models: although cytokine secretion was observed in all cases, OIS fibroblasts secreted much higher levels of IL-6, IL-8 and Gro-α than those incubated with $H_2O_2$ or doxorubicin (Supplementary Fig. S1); also a significant increase in *CDKN2A*
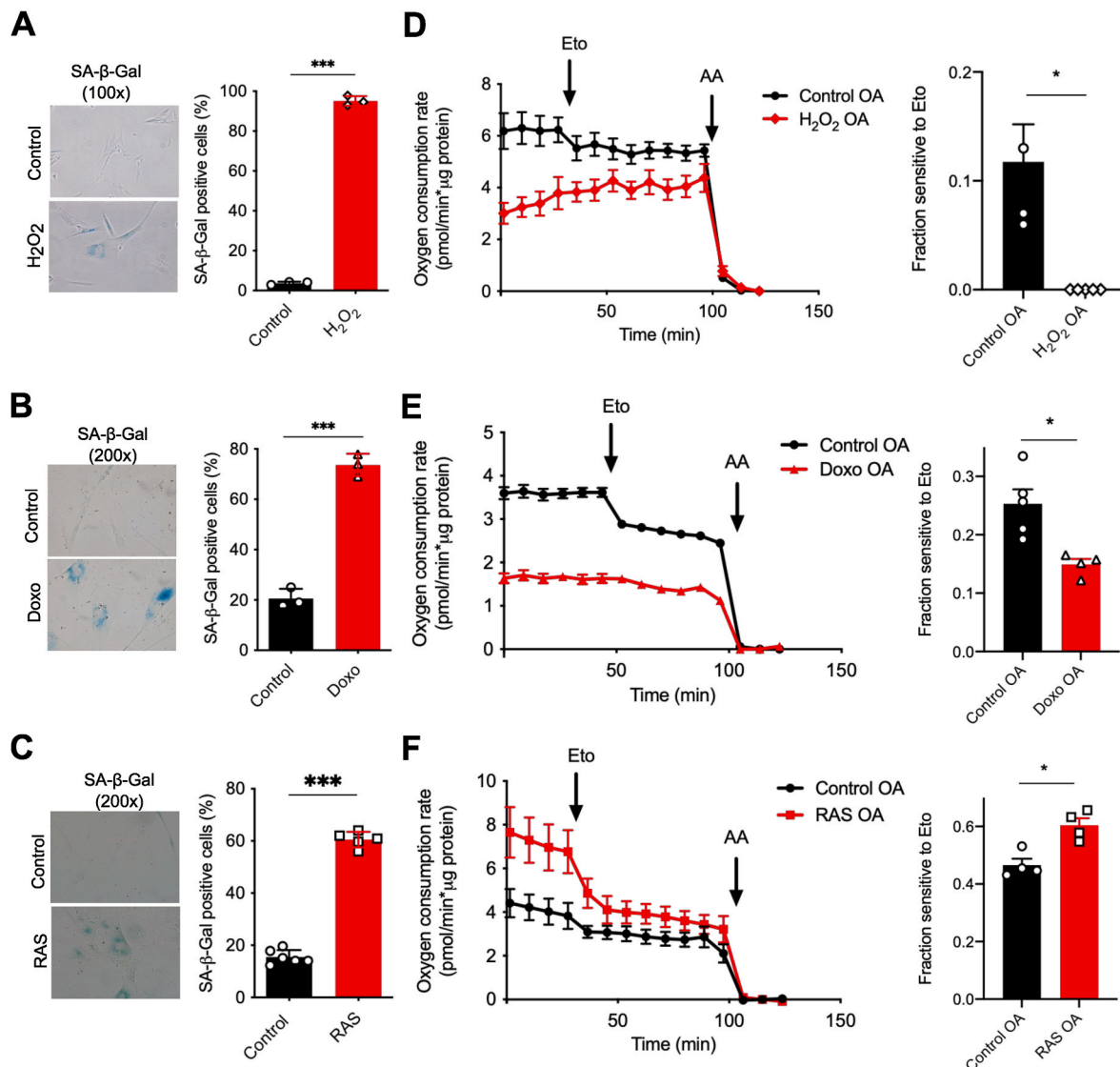


Fig. 1. Senescence induction and fatty acid oxidation in human fibroblasts exposed to different stimuli. Early passage IMR-90 human fibroblasts were incubated with the different senescence inducing stimuli. Measurements were made 14 days after treatment. **A)** Fibroblasts were exposed to $H_2O_2$ in complete media (600 μM) for 2 h, (two exposures separated by a five day interval). **(B)** Fibroblasts were exposed to doxorubicin 0.2 μM for 24 h (Doxo) or the vehicle DMSO (Control) in complete media. **(C)** Fibroblasts were transduced with lentiviral particles containing a plasmid coding for the H-RAS[G12V] oncogene (RAS) or a control plasmid (Control), and selected with puromycin. **(A, B, C)** SA-β-Gal activity was determined. **(D, E, F)** Oxygen consumption rate (OCR) was measured in a Seahorse XFe24 in media containing an oleate:BSA conjugate (0.1 mM:0.2% m/v). The CPT1 inhibitor etomoxir (Eto, 100 μM) and complex III inhibitor Antimycin A (AA, 2.5 μM) were sequentially added to the culture. Fatty acid oxidation was determined as the fraction of the OCR sensitive to etomoxir, calculated as the ratio between etomoxir sensitive OCR and basal OCR. Results are the mean ± SEM. Significant differences between senescent cells and the control condition were determined with Student's t-test. *P < 0.05 (n = 3–5).

(p16-INK4) was present in OIS and doxorubicin-induced senescent cells, but not in $H_2O_2$ treated cells. Differences in the activation of the DDR were also observed between models and are discussed later (Fig. 4 and Supplementary Fig. S1).

We measured oxygen consumption rates in the presence of oleate conjugated to BSA with or without etomoxir, an inhibitor of carnitine palmitoyltransferase 1 (CPT1). When cells were exposed to $H_2O_2$ or doxorubicin, a decrease in oxygen consumption rate dependent on fatty acid oxidation (sensitive to etomoxir) was observed, with respect to the control condition (Fig. 1D and E).

On the contrary, in OIS fatty acid oxidation increased (Fig. 1F), along with the phosphorylation of ACC in serine 79 by AMPK, as previously described [9,13] (Supplementary Fig. S2). Phosphorylation of ACC in this residue inhibits enzyme activity, decreasing malonyl-CoA levels and promoting CPT1-dependent fatty acid import into mitochondria. This phenomenon was not observed in $H_2O_2$- or doxorubicin-induced senescence, were etomoxir sensitive respiration was undetectable or

lower (Fig. 1D and E) and ACC phosphorylation was the same as in control cells (Supplementary Figs. S2A and S2B). Of note, in OIS cells mitofusin 1 and 2 levels were decreased (Supplementary Fig. S3), this has been recently reported to increase CPT1 activity as well [33].

### 2.2. Mitochondrial bioenergetics in senescent lung fibroblasts induced with different stimuli

We then measured mitochondrial respiration in the different models of cell senescence, in media containing glucose, pyruvate and glutamine. In $H_2O_2$-induced senescent cells, we observed a small but significant increase in ATP-independent respiration (Fig. 2A) and accordingly a decrease in coupling efficiency and respiratory control ratio with respect to the control (Table 1). In doxorubicin-induced senescent cells, a lower ATP-dependent respiration rate (Fig. 2B), coupling efficiency and respiratory control ratio were found (Table 1), as well as a small but significant decrease in maximal respiration rate relative to control non-
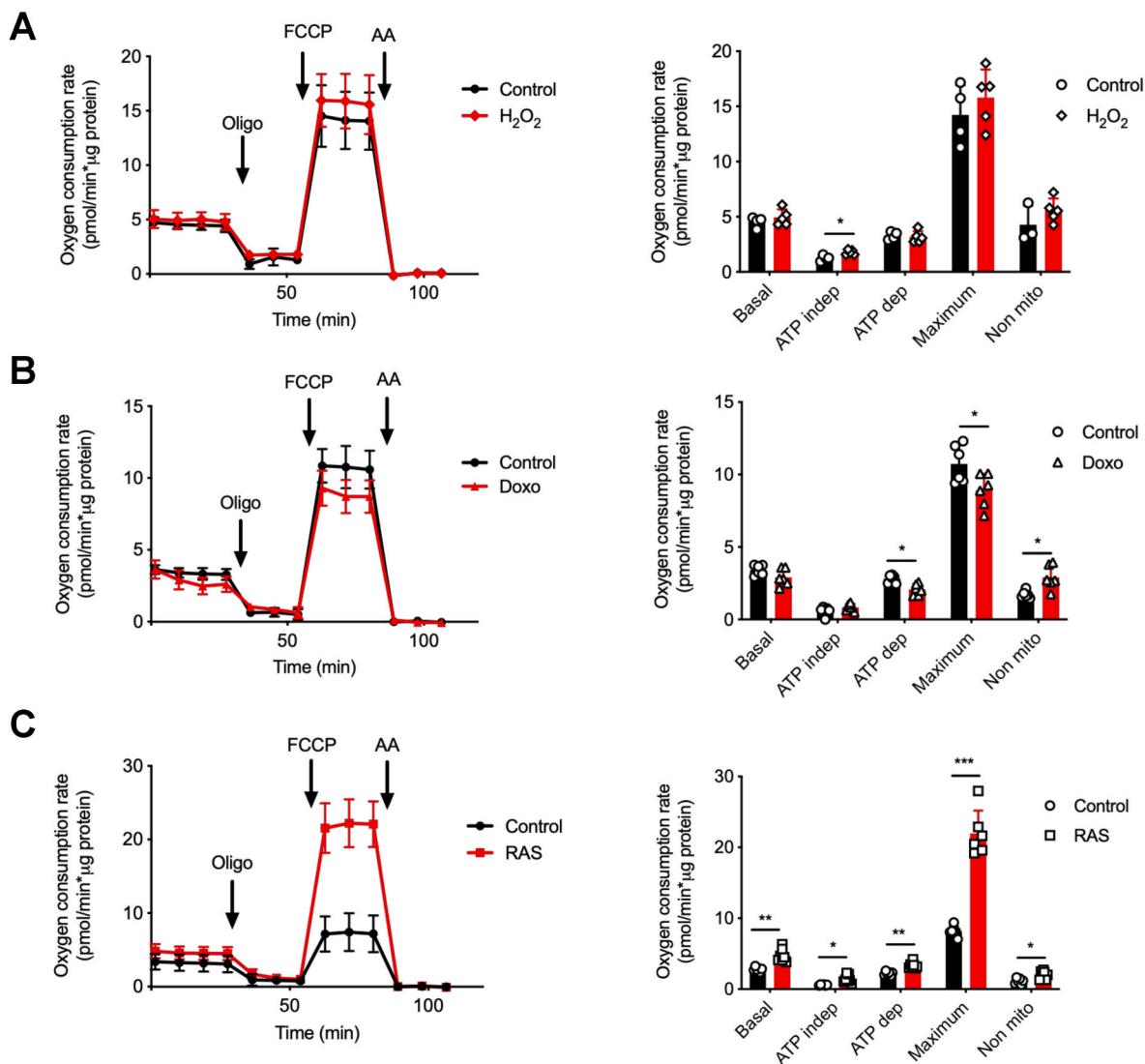


**Fig. 2. Mitochondrial bioenergetics in senescent human fibroblasts induced with different stimuli.** Early passage IMR-90 human fibroblasts were incubated with the different senescence inducing stimuli, and after 14 days oxygen consumption rate (OCR) was measured in the Seahorse XFe24 in media containing glucose 5 mM, pyruvate 1 mM, glutamine 2 mM. The ATP synthase inhibitor oligomycin (Oligo, 0.5 μM), the uncoupler FCCP (1 μM) and complex III inhibitor antimycin A (AA, 1 μM) were sequentially added to the culture. Respiratory parameters were determined as described in the Methods section. **(A)** Fibroblasts were exposed to $H_2O_2$ in complete media (600 μM) for 2 h, (two exposures separated by a five day interval) (n = 4–5). **(B)** Fibroblasts were exposed to doxorubicin 0.2 μM for 24 h (Doxo) or the vehicle DMSO (Control) in complete media (n = 6). **(C)** Fibroblasts were infected with lentiviral particles containing a plasmid coding for the H-RAS$^{G12V}$ oncogene (RAS) or a control plasmid (Control). Cells were selected with puromycin (n = 6–7). Results are the mean ± SD. Significant differences between senescent cells and the control condition were determined with Student's t-test. *P < 0.05, **P < 0.001, ***P < 0.0001.

**Table 1**

**Mitochondrial respiratory indexes**. Coupling efficiency, spare respiratory capacity and respiratory control ratio were calculated as described in Methods, considering the values shown in Fig. 2 and Supplementary Fig. S4H. Results are the mean ± SD. Significant differences between senescent cells and the control condition were determined with Student's t-test. *P < 0.05, ***P < 0.0001.

| Indexes | Control | H₂O₂ | Control | Doxo | Control LV | RASLV | Control (Early) | Rep Sen |
|---|---|---|---|---|---|---|---|---|
| Coupling efficiency | 0.83 ± 0.04 | 0.71 ± 0.02* | 0.73 ± 0.04 | 0.64 ± 0.01* | 0.79 ± 0.01 | 0.73 ± 0.02* | 0.72 ± 0.01 | 0.55 ± 0.03** |
| Spare respiratory capacity | 3.1 ± 0.05 | 3.1 ± 0.1 | 3.1 ± 0.4 | 3.2 ± 0.2 | 2.9 ± 0.03 | 4.8 ± 0.09*** | 1.4 ± 0.3 | 1.4 ± 0.3 |
| Respiratory control ratio | 15 ± 1 | 11 ± 1* | 11 ± 1 | 8.9 ± 0.6* | 13.7 ± 0.5 | 18 ± 2* | 5 ± 1 | 3.1 ± 0.8* |

senescent fibroblasts (Fig. 2B). These results are in agreement with a decrease in mitochondrial bioenergetics in senescent cells induced by these stimuli.

Additionally we studied mitochondrial bioenergetics in replicative senescent cells, obtained after serial passaging of the culture as shown previously [32]. Replicative senescent cells (60% positive for SA-β-Gal staining), showed an increase in fatty-acid dependent oxygen consumption rate with respect to early passage cells. This was not accompanied by ACC or AMPK phophorylation, but might be linked to lower ACC levels reported previously [32]. However, basal and ATP-dependent respiration, as well as coupling efficiency and respiratory control ratio were lower in senescent cells than in early passage fibroblasts (Supplementary Fig. S4 and Table 1). Differences between conditions could not be attributed to proliferation arrest, since proliferating and quiescent fibroblasts had similar respiratory parameters as

well as fatty acid-dependent oxygen consumption rates (Supplementary Fig. S5).

However, when senescence was induced by expression of the RAS oncogene a marked and significant increase could be observed in all respiratory parameters (Fig. 2C). Maximum respiration rate increased 2.7-fold, in agreement with reports of an increase in mitochondrial biogenesis [9], and the spare respiratory capacity revealed a higher capacity to respond to increases in energy demands (Table 1). As observed for the other two models of senescence, coupling efficiency was reduced in agreement with reports of mitochondrial membrane depolarization [9]. Nevertheless the respiratory control ratio (RCR), was significantly higher in OIS fibroblasts than control cells (Table 1), supporting an overall increase in mitochondrial bioenergetics [34].

In agreement, mtDNA/nDNA ratio had a 5.6-fold increase in oncogene-induced senescence with respect to control cells (6 ± 3 vs 1 ±
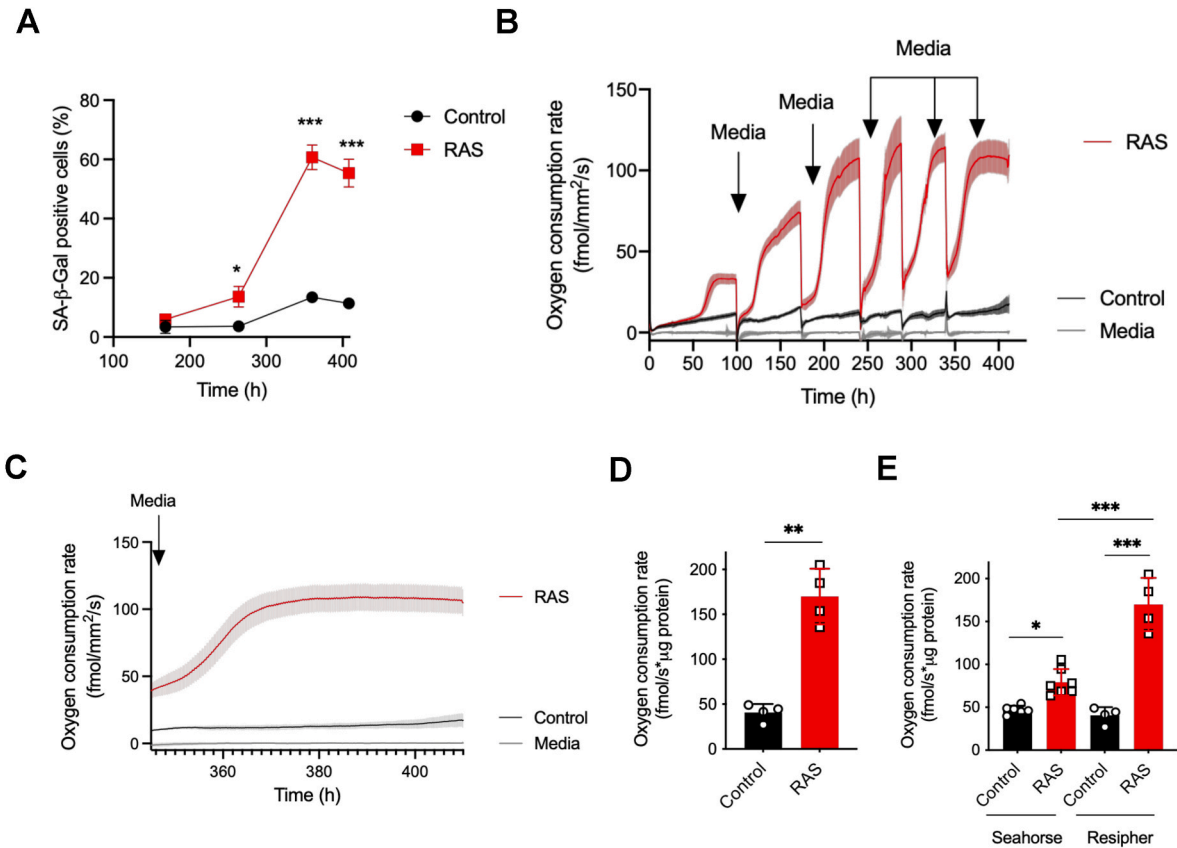


**Fig. 3. Time course of basal respiration of oncogene-induced senescent human fibroblasts.** Early passage IMR-90 human fibroblasts were transduced with lentiviral particles carrying a Control or H-RAS^G12V (RAS) containing plasmid, and selected with puromycin. **(A)** SA-β-Gal activity was measured at different time points (n = 3). **(B)** Oxygen consumption rate (OCR) was measured continuously using a Resipher instrument. Measurements were made in complete media, in a CO₂ containing stove, from the day the selection started. Oxygen consumption rate of Control and RAS cells from day 1 (0 h) to day 17 (410 h) after selection. Wells including only media were measured to control for cell-independent OCR. Media was changed every 2–3 days (arrows). **(C)** Basal oxygen consumption rate of senescent and non-senescent cells from day 14–17 (345–410 h) after the addition of puromycin **(D)** Basal respiration at 400 h was normalized by protein content in the wells. **(E)** Basal respiration normalized by protein content 14 days after the addition of puromycin, measured using the Seahorse XFe24 or Resipher instruments was compared. Results are the mean ± SD. Significant differences between conditions were determined with Student's t-test. *P < 0.05, **P < 0.001, ***P < 0.0001 (n = 4).

0.4, P = 0.0035), while no significant changes were observed for doxorubicin treated cells (1 ± 0.7 vs 1 ± 0.3, P = 0.95).

A similar increase in mitochondrial energy metabolism, with the consequent increase in respiration rates, was reported in human fibroblasts where senescence was induced by the BRAF$^{V600E}$ oncogene [12] and in therapy-induced senescence in cancer cells [14,15].

### 2.3. Temporal changes in oxygen consumption rate following the induction of senescence by RAS

To further explore mitochondrial respiration in oncogene-induced senescent cells, we followed the basal oxygen consumption rate from the day cells were selected with puromycin (one day after transduction with lentiviral particles), until the senescent phenotype was fully stablished and a maximum of 60% SA-β-Gal positive cells was obtained (Fig. 3A). We used the Resipher system, that measures oxygen consumption in a culture dish placed inside the carbon dioxide ($CO_2$) incubator in complete culture media, containing fetal bovine serum (FBS).

The basal oxygen consumption of rate of cells expressing the RAS oncogene started increasing and became significantly higher than the control approximately two days (48 h) after selection, and maximum respiration rates were achieved around day twelve (288 h) (Fig. 3B). At the end of the experiment protein content was determined and respiration normalized, revealing that basal respiration rates were 4-fold higher in senescent than control cells (Fig. 3D).

Analysis of the data showed that control cells achieved a steady oxygen consumption rate 6 h after changing the media, while senescent cell cells required around 30 h to stabilize (Fig. 3C). This observation raised doubts regarding a possible underestimation of the oxygen consumption rates of RAS-induced senescent cell obtained with the Seahorse XFe24 (Fig. 2C), since it is typically measured one to 2 h after changing the media, and in absence of FBS. Comparison of the basal respiration rates obtained with the two instruments fourteen days after selection revealed similar values for control cells (Fig. 3E). However, significantly higher rates were obtained for senescent cells measured with the Resipher than the Seahorse XFe24 (Fig. 3E).

### 2.4. Mitochondrial bioenergetics time course in oncogene-induced senescence and $H_2O_2$-induced senescence

Additionally, we confirmed that oncogene-induced senescence was accompanied by an increase in mitochondrial bioenergetics in skin fibroblasts (BJ) carrying the H-RAS$^{G12V}$ oncogene fused to the ligand binding domain of the estrogen receptor (ERRAS). In these cells RAS expression was induced upon incubation with 4-hydroxytamoxifen (4OHT), and led to an increase in senescence markers, such as phosphorylated ataxia-telangiectasia mutated kinase (ATM) (Ser1981), p53, p16 and SA-β-Gal (Fig. 4A and B). Respiration rates also increased in cells expressing the RAS oncogene, as well as AMPK and ACC phosphorylation (Fig. 4C and D), supporting the observations made in IMR-90 fibroblasts undergoing OIS (Fig. 2 and Supplementary Fig. 2) and previous reports [9,13,26]. Six days after exposure to 4OHT senescent fibroblasts demonstrated significant increases in all respiratory parameters and indexes (Fig. 4D and Table 2) with respect to the control, indicative of a rise in mitochondrial bioenergetics. On the other hand practically no changes could be observed in the respiratory parameters of fibroblasts exposed to $H_2O_2$ when compared to control cells, at different time points (Fig. 4E and F).

The time course observed for OIS is in agreement with time dependent gene expression profiles for senescent cells reported by Hernández-Segura et al. [6], showing enrichment in the Tricarboxylic acid (TCA) cycle (also known as Krebs cycle or citric acid cycle) and respiratory electron transport pathways at intermediate times, around 10 days after exposure to the senescence inducing stimuli [6].

### 2.5. Increased mitochondrial respiration rate is associated with AMPK activation and the acquisition of a secretory phenotype

To better understand the increase in mitochondrial oxygen consumption rates observed in OIS, we studied what happened after removing the ERRAS inducer (4OHT) from the senescent culture. Retrieving 4OHT from the culture on day 11, reduced RAS levels but did not affect p16 or pRb hypophosphorylation (Supplementary Fig. S6). Though some cells might have evaded senescence in this conditions [35], our results suggest proliferation was not restored in most of the cell culture.

BJ fibroblasts were incubated with 4OHT for eleven days in order to induce senescence in the culture. Half of the dishes were then switched to the vehicle (methanol) for nine days (Sen - RAS), while the other half continued under 4OHT stimulation (Sen + RAS). Controls were incubated with methanol throughout the experiment (Fig. 5A).

Remotion of 4OHT reduced RAS significantly, to a similar level than that of control cells, reducing extracellular signal-regulated kinases 1/2 (ERK1/2) phosphorylation (Thr202/Tyr204) and thus the mitogen activated protein kinase (MAPK) signaling pathway (Fig. 5B). A significant decrease in p21 but not in p16 levels was observed (Fig. 5B).

Regarding the SASP, we observed that interleukin 8 (IL-8) secretion was significantly higher than the control only in senescent cells carrying RAS (Sen + RAS) (Fig. 5C). A similar profile was observed for p65 a subunit of nuclear factor-κB (NF-κB), master regulator of the SASP [36, 37] (Fig. 5B). IL-8 secretion by senescent BJ skin fibroblasts was lower than in IMR-90 lung fibroblasts, in agreement with previous reports that show tissue-dependent differences in the SASP [6,38].

Assessment of metabolic parameters revealed that lack of RAS expression also reduced AMPK-mediated phosphorylation of ACC (Ser79) (Fig. 6A), as well as all respiratory parameters (Fig. 6B). In fact, a similar profile to that of p65 was observed for ACC phosphorylation, and p-ACC presented a strong correlation with p65 levels (Pearson coefficient r = 0.9808, P < 0.0001).

To explore if the changes observed in metabolic pathways were required to sustain the SASP OIS fibroblast were incubated with the AMPK inhibitor compound C (CC, dorsomorphin) [39]. As shown in Fig. 6 incubation with CC (10 μM) suppressed ACC phosphorylation, confirming AMPK inhibition (Fig. 6C). Compound C reduced basal, ATP-dependent, ATP-independent and maximum respiration rates (Fig. 6D) in senescent cells, as well as the secretion of various components of the SASP (Fig. 6E). Interestingly, addition of oligomycin an inhibitor of mitochondrial ATP synthase, also inhibited cytokine secretion (Fig. 6E). These results support AMPK activation as a key event in OIS, that coordinately regulates nutrient catabolism and the SASP.

Accordingly, IMR-90 senescent fibroblasts induced by $H_2O_2$ or doxorubicin, that did not present AMPK activation (Supplementary Fig. S2) or an increase in mitochondrial respiration rates (Figs. 1 and 2), had a much lower secretion of IL-6, IL-8 and Gro-α when compared to OIS cells (Supplementary Fig. S1).

To further explore the connection between the SASP and mitochondrial respiration rates we used the IκB kinase (IKK) inhibitor BAY 11–7082 (BAY), that prevents the phosphorylation and degradation of NF-κB inhibitor (IκB), retaining NF-κB in the cytosol and inhibiting its transcriptional activity. Incubation of RAS-induced senescent cells with BAY (10 μM) for 24 h successfully inhibited IL-6 and IL-8 secretion by OIS cells (Supplementary Fig. S7), and decreased ATP-dependent respiration in senescent cells (Supplementary Fig. S7). Suggesting that mitochondria-derived ATP fuels the synthesis and secretion of cytokines by senescent cells. This results are in agreement with our previous reports, showing that inhibition of mitochondrial fatty acid oxidation reduces the SASP [13].

A persistent DNA damage response (DDR), involving ATM activation has also been reported as a requirement for the establishment of the SASP [40], and mitochondrial biogenesis [10]. Comparison of DDR activation in the different models showed that RAS-induced senescent
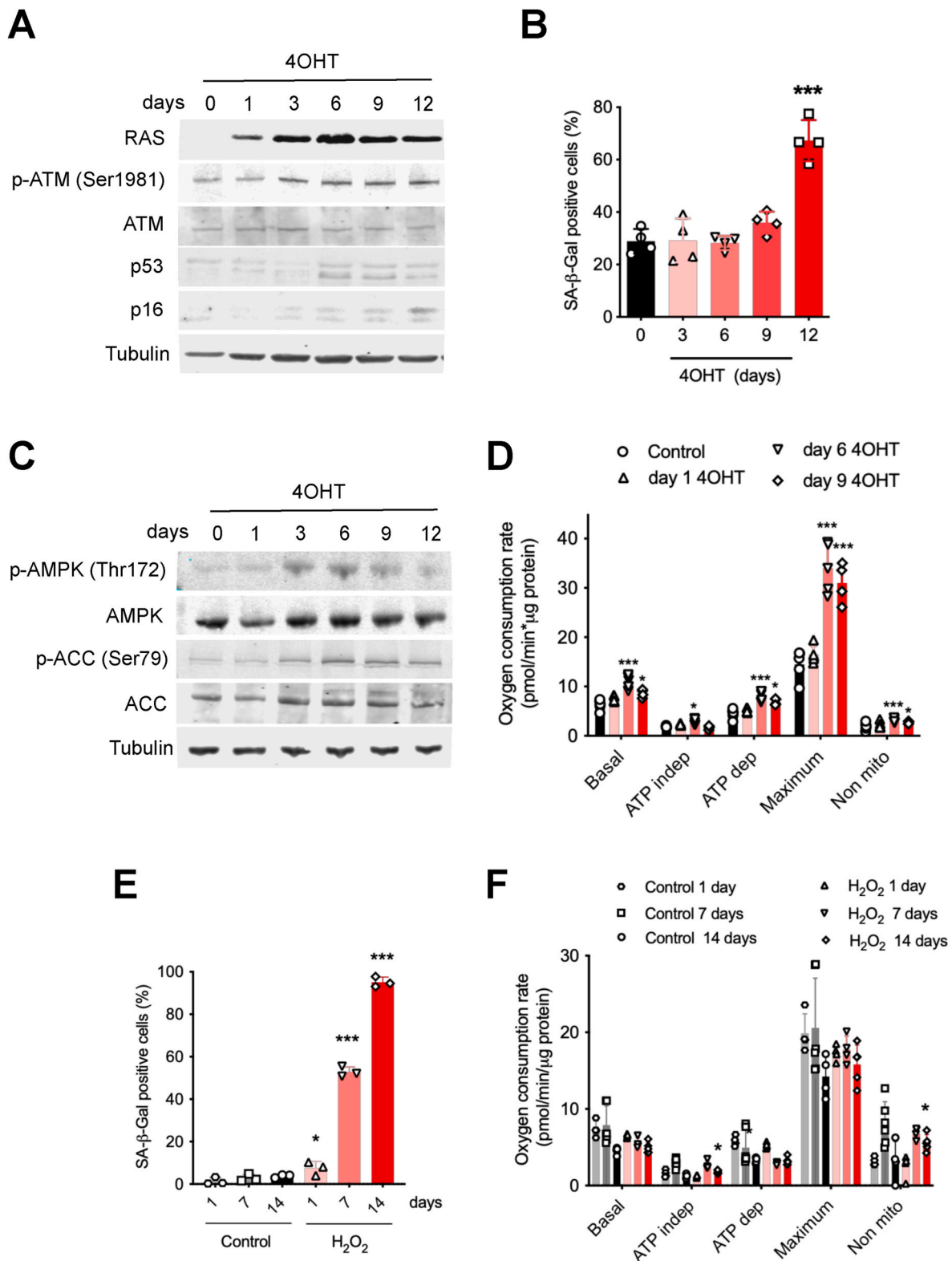
**Fig. 4. Time course of mitochondrial bioenergetics in oncogene-induced senescent human fibroblasts. (A–D)** Early passage BJ human fibroblasts carrying ERRAS fusion protein were cultured. Measurements were made at different time points after the addition of 4OHT (200 nM). **(A)** Representative western Blots (WB) of RAS, phosphorylated ATM (p-ATM) (Ser1981), ATM, p53, p16 and tubulin (loading control). **(B)** SA-β-Gal staining (n = 4). **(C)** Representative WB of phosphorylated AMPK (p-AMPK) (Thr172), AMPK, phosphorylated ACC (p-ACC) (Ser79), ACC, and tubulin as loading control. **(D)** Oxygen consumption rate (OCR) was measured and respiratory parameters determined as described in Fig. 2. Results are the mean ± SD (n = 4–5). **(E–F)** IMR-90 fibroblasts were exposed to $H_2O_2$ in complete media (600 μM) for 2 h, (two exposures separated by a five day interval). Measurements were made at different time points after the last addition of the oxidant. **(E)** SA-β-Gal activity (n = 3). **(F)** OCR was measured and respiratory parameters determined as described in Fig. 2 (n = 3–4). Results are the mean ± SD. Significant differences between senescent cells and the control condition were determined with ANOVA and Dunnett post-hoc for multiple comparisons (B and D), or Student's t-test (E and F). *$P < 0.05$, **$P < 0.001$, ***$P < 0.0001$.

**Table 2**
Mitochondrial respiratory indexes in BJ fibroblasts expressing ERRAS. Coupling efficiency, spare respiratory capacity and respiratory control ratio were calculated, as described in Methods, considering the values shown in Fig. 4D. Results are the mean ± SD. Significant differences between senescent cells and the control condition were determined by one-way ANOVA *P < 0.05, **P < 0.001 (n = 4–5).

| Indexes | Control | +4OHT | | |
|---|---|---|---|---|
| | | Day 1 | Day 6 | Day 9 |
| Coupling efficiency | 0.7 ± 0.05 | 0.69 ± 0.01 | 0.74 ± 0.03 | 0.8 ± 0.04* |
| Spare respiratory capacity | 2.0 ± 0.1 | 2.1 ± 0.2 | 3.1 ± 0.2** | 3.4 ± 0.4** |
| Respiratory control ratio | 7 ± 1 | 7 ± 1 | 12 ± 2** | 17 ± 2** |

cells presented persistent activation of this signaling cascade, evidenced by ATM phosphorylation several days after the induction of RAS expression (Fig. 4A). While, exposure to $H_2O_2$ or doxorubicin only led to a transient activation of the DDR, where an increase in ATM phosphorylation was observed 24 h after exposure to the genotoxic agent, but then decayed and became undetectable at longer times (Supplementary Fig. S1).

## 2.6. Catabolic pathways in oncogene-induced senescent fibroblasts

To better understand the bioenergetics of RAS-induced senescent fibroblasts we compared the metabolites detected in senescent and non-senescent cells in our previous work [13]. Several glycolytic pathway intermediates (glucose, fructose 1,6-biphosphate/glucose 1,6-biphosphate, 3-phsphoglycerate, 2-phosphoglycerate and phosphoenolpyruvate) were significantly higher in RAS-induced senescent cells compared to control cells (Supplementary Fig. S8), suggesting an overall increase in this pathway as previously reported [26,27]. Similar
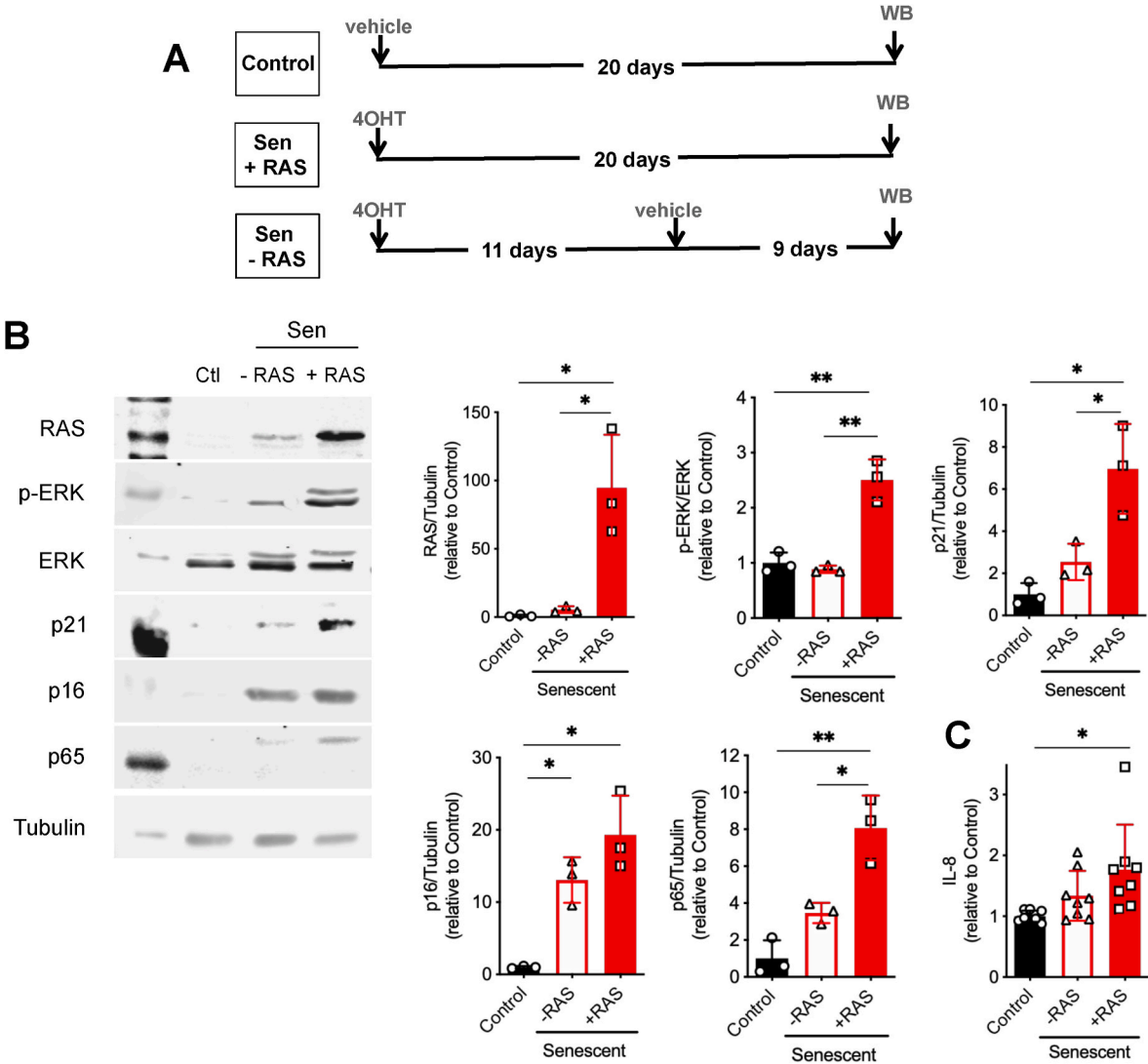


**Fig. 5. RAS levels and the senescent phenotype.** Early passage BJERRAS fibroblasts were incubated 4OHT (200 nM) (Sen + RAS) or the vehicle methanol (Control) for 20 days. A third group was exposed to 4OHT (200 nM) for 11 days, and on day 12 when the cells had acquired a senescent phenotype, the cultures were switched to vehicle and incubated in these conditions for 8 more days (Sen - RAS). **(A)** Scheme showing the culture conditions of the three groups: Control, Sen + RAS, Sen - RAS. **(B)** Representative western blots showing the levels of RAS, phosphorylated ERK (p-ERK) (Thr202/Tyr204), ERK, p21, p16, p65 and tubulin as loading control. Graphs show the quantification of the different proteins normalized to the control condition. Results are the mean ± SD (n = 3). **(C)** IL-8 secretion assessed by ELISA, normalized considering cell protein content (μg) (n = 8) and relative to the control. Significant differences between senescent cells with and without RAS and the control condition were determined with one-way ANOVA, and Tukey post-hoc for multiple comparisons *P < 0.05, **P < 0.001, ***P < 0.0001.
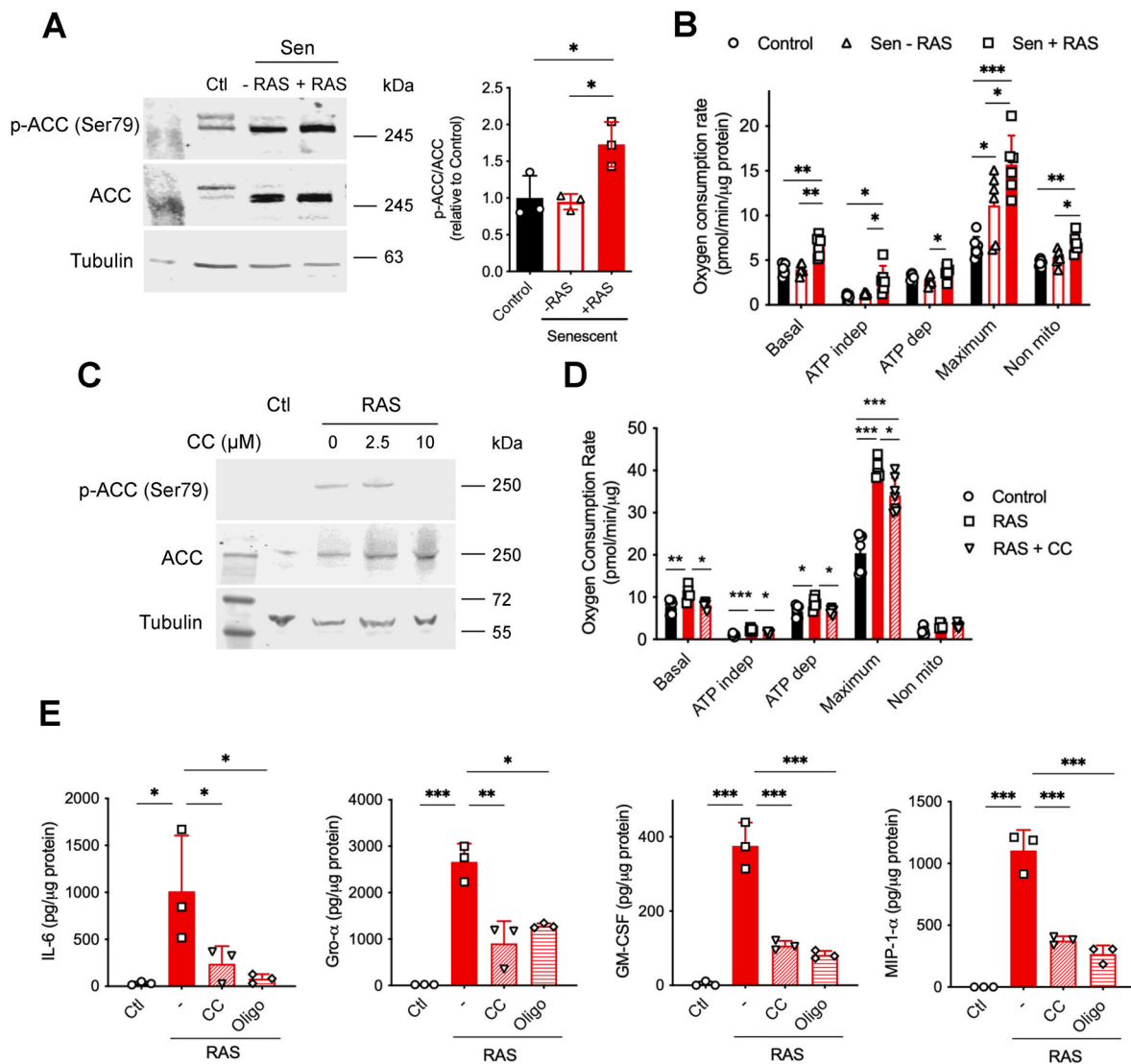
**Fig. 6. AMPK activation drives the increase in cell respiration and the SASP in OIS. (A)** Early passage BJERRAS fibroblasts were incubated as described in Fig. 5. Representative western blots showing the levels of phosphorylated ACC (p-ACC) (Ser79), ACC, and tubulin as loading control. The graph shows the p-ACC/ACC ratio relative to the control condition. Results are the mean ± SD (n = 3). **(B)** Oxygen consumption rate (OCR) was measured and respiratory parameters determined as described in Fig. 2. **(C)** IMR-90 human fibroblasts were transduced with lentiviral particles containing H-RAS$^{G12V}$ oncogene (RAS) or a control plasmid (Ctl). Senescent cells were incubated with CC (10 μM) for 6 h and western blots preformed with antibodies against p-ACC (Ser79), ACC, and tubulin as loading control. **(D)** Oxygen consumption rate (OCR) was measured and respiratory parameters determined for IMR-90 fibroblasts incubated with CC (10 μM) or vehicle (n = 6–7). **(E)** Cytokine secretion was assessed by ELISA, and normalized considering cell protein content (n = 3) for IMR-90 fibroblasts incubated with CC (10 μM) or oligomycin (1 μM) for 6 h (n = 6–7). Results are the mean ± SD. Significant differences between senescent cells with and without RAS and the control condition were determined with one-way ANOVA, and Tukey or Dunnett's post-hoc for multiple comparisons *P < 0.05, **P < 0.001, ***P < 0.0001.

observations were made for replicative senescent cells (Fig. S9). However, lactate levels were reduced in OIS (Fig. 7A) indicating that pyruvate formed in the glycolytic pathway, is perhaps oxidized to acetyl-CoA rather than reduced to lactate. Accordingly, subunits E1α and E2 of the pyruvate dehydrogenase complex (PDH) were 3.5 and 7.5-fold higher in senescent than non-senescent cells and E1β was undetectable in control cells, but present in senescent cells (Fig. 7B–D).

Assessment of metabolites from the TCA cycle showed OIS cells had significantly lower levels of α-ketoglutarate and higher levels of succinate, malate and fumarate levels, than control cells (Fig. 7A). No differences were found in pyruvate or citrate levels; while acetyl-CoA, *cis*-aconitate, isocitrate, succinyl-CoA and oxaloacetate were not detected.

We reasoned that the decrease in α-ketoglutarate could be due to mitochondrial aconitase (ACO2) inactivation, since the iron-sulfur cluster in the active site makes the enzyme very sensitive to oxidants, in particular to superoxide radical ($O_2^{\cdot-}$) [41–44], and reactive oxygen

species are known to increase in senescence [9,23]. Thus, we obtained mitochondria-enriched and cytoplasm-enriched subcellular fractions, and measured aconitase activity following the rate of conversion of isocitrate to *cis*-aconitate inhibitable by fluorocitrate, a well-known aconitase inhibitor [45] (Supplementary Fig. S10). Aconitase activity was reduced 43% in the mitochondrial compartment but not in the cytoplasm of senescent cells (Fig. 7E). Incubation of mitochondrial fractions of senescent cells with iron and a reducing agent in anoxic conditions resulted in a 16 ± 2% recovery of aconitase activity.

Considering aconitase reactivation in senescent cells, as well as reported values for control cells (10%), and applying the equation presented in the Material and Methods section [41], we estimated a 40 ± 20% increase in superoxide steady-state levels in OIS cells with respect to control cells. In agreement, intracellular oxidant levels determined measuring the oxidation of chloromethyl-2′,7′-dichlorodihydrofluorescein (CM-H$_2$DCF) to the fluorescent probe chloromethyl-2′,
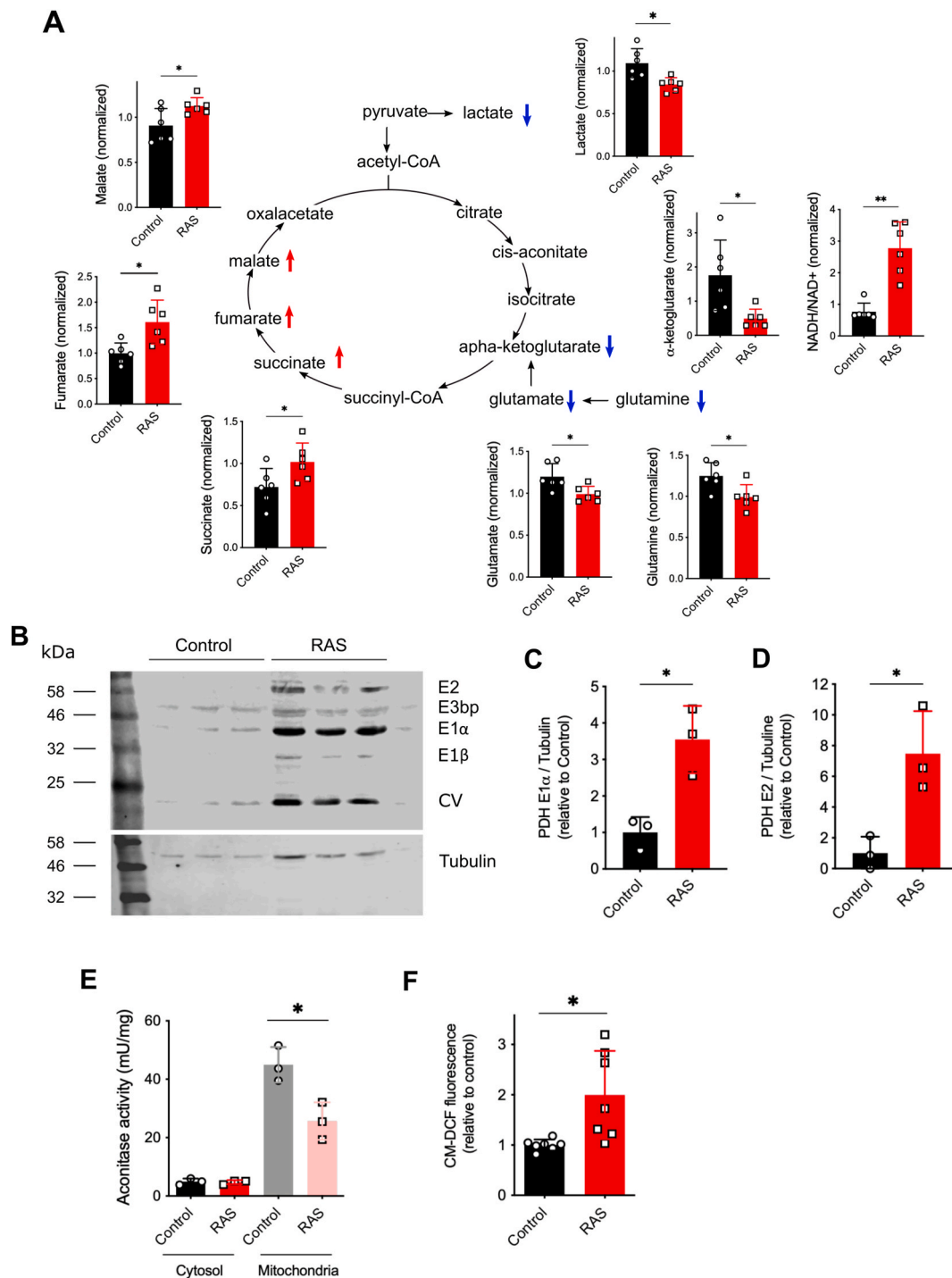
**Fig. 7. Mitochondrial metabolic features of oncogene-induced senescent human fibroblasts.** Early passage IMR-90 human fibroblasts were transduced with lentiviral particles containing a plasmid coding for the H-RAS$^{G12V}$ oncogene (RAS) or a control plasmid (Control), and selected with puromycin. Measurements were made 14 days after transduction. **(A)** Data from metabolomic experiments reported in Ref. [13] (n = 6). **(B)** Representative WB for Pyruvate dehydrogenase complex subunits. **(C and D)** Graphs show the quantification of the subunits E1α, and E2 proteins relative to tubulin and normalized to the control condition. Results are the mean ± SD (n = 3). **(E)** Aconitase activity was determined by spectrophotometric techniques (n = 3). **(F)** Intracellular oxidant levels measured assessing chloromethyl-2′,7′-dichlorofluorescein (CM-DCF) fluorescence intensity by flow cytometry analysis (n = 7), the geometric mean fluorescence intensity relative to the control condition is shown. Results are the mean ± SD. Significant differences between senescent cells and the control condition were determined with Student's t-test. *P < 0.05, **P < 0.001.

7′-dichlorofluorescein (CM-DCF), were increased two-fold (Fig. 7F).

Assessment of other metabolites revealed a decrease in glutamate, glutamine, γ-aminobutyric acid (GABA), and propionyl carnitine in senescent cells (Fig. 7A and Supplementary Fig. S8), suggesting these metabolites might also play a role fueling the TCA cycle.

We also analyzed the metabolites detected in replicative senescent and early passage fibroblasts measured previously [13]. As observed for OIS fibroblasts, several glycolytic pathway intermediates and citrate were significantly higher, and α-ketoglutarate was lower in replicative senescent cells compared to early passage cells (Supplementary Fig. S9).

## 2.7. Alternative routes for acetyl-CoA in oncogene-induced senescent fibroblasts

To explore other potential outcomes for citrate we studied ATP-citrate lyase (ACLY), an enzyme that catalyzes the cleavage of citrate into oxalacetate and acetyl-CoA in the cytoplasm and nucleus [46,47]. Phosphorylation of ACLY in serine 455, is catalyzed by protein kinase A (PKA) or Akt (PKB) [48,49], and is associated with an increase in lipid synthesis and histone acetylation [46,47]. In fact, upon activation of the DNA damage response p-ACLY has been shown to promote histone H3 acetylation in lysine 9 (H3K9Ac) and lysine 56 (H3K56Ac) near double strand breaks, affecting chromatin structure and gene experession [50].

As shown in Fig. 8, a 4.7-fold increase in p-ACLY (Ser 455) levels and a 6.3-fold increase in p-ACLY/ACLY ratio was found in senescent versus non-senescent cells (Fig. 8A–D). ACLY phosphorylation also increased in BJ fibroblasts upon induction of oncogene expression with 4OHT (Fig. 8E). A similar profile was observed for p-ACC (Ser 79) (Fig. 8E). In this setting, where p-ACLY promotes acetyl-CoA export from mito-chondria and ACC phosphorylation inhibits lipid synthesis, acetyl-CoA might participate in other reactions, for example, protein lysine acetyl-lation (AcLys). Accordingly, acetylation of H3 in lysine 9 (H3K9Ac) was higher in OIS than in control cells, and incubation with the ACLY in-hibitor NDI-091143 (NDI) [51,52] resulted in a decrease in H3K9Ac (Fig. 8F and G). Incubation with the ACLY inhibitor also resulted in a decrease in pro-inflammatory cytokine secretion by senescent fibro-blasts (Fig. 8H and I).

Finally, we looked at Sirtuin 6 (SIRT6) levels, since this enzyme can catalyze the $NAD^+$-dependent deacetylation of histone H3 (H3K9Ac and H3K56Ac) among other targets [53–55]. *SIRT6* expression and protein levels were increased in IMR-90 OIS senescent cells (Fig. 8J–L) and in OIS BJ fibroblasts (Sen + RAS) (Supplementary Fig. S11). In our experimental conditions the SIRT6 substrate $NAD^+$ was reduced, NADH was unchanged, and $NAD^+$ precursors nicotinamide and nicotinamide riboside were increased in senescent cells with respect to the control [13] (Supplementary Fig. S8). However, reports by others show an in-crease in both $NAD^+$ and $NAD^+$ precursors in OIS cells, associated to higher activity of the $NAD^+$ salvage pathway [26,27]. Sirtuin 6 partic-ipates in the activation of the DNA damage response [56], regulates cell catabolism [57–60] and inflammation [61], and could account for the coordinated regulation of these processes in senescent cells.

## 3. Discussion

Mitochondria are required for the secretion of multiple pro-inflammatory factors by senescent cells [10]. Inhibition of catabolic routes such as fatty acid oxidation [13], mitochondrial biogenesis or mitochondrial fusion reduces several senescent markers, including the SASP [10,12–14,24]. Impairment of mitochondrial respiration or loss of mtDNA per se can induce senescence in young proliferating fibroblasts [31,62]. However, senescent cells induced by loss of mtDNA (rho cells) present a characteristic SASP devoid of many proinflammatory factors [31]. In line with these observations, recent reports show that release of mtDNA and mt-dsRNA to the cytoplasm activate cyclic GMP-AMP syn-thase and stimulator of interferon genes protein (cGAS-STING) and MAVS pathways, respectively, and these proinflammatory pathways drive the SASP [16,24]. Here we show that inhibition of AMPK, a master regulator of energy metabolism, strongly affects the SASP in OIS, underscoring the potential of mitochondria as targets to modulate the SASP.

Additionally, our study provides a careful description of mitochon-drial catabolic pathways in OIS, along with a comparison with other models of senescence. To characterize and compare mitochondrial respiration and oxidative phosphorylation pathways in the different models we compared their respiratory indexes. Respiratory indexes are determined as ratios between the respiratory rates, and are therefore internally normalized and independent of cell number or protein mass

[34]. In all cases IMR-90 senescent cells showed a small but significant decrease in coupling efficiency (Table 1). This index considers the fraction of mitochondrial respiration that is directly linked to ATP synthesis, and a decrease indicates dissipation of the proton gradient though processes that do not involve ATP synthase [34]. Among these events we can find an increase in the permeability of the mitochondrial inner membrane (MIM) due to damage or activity of uncoupling proteins (UCP), but also transport of metabolites across the MIM such as $Ca^{2+}$, pyruvate (that is co-transported to the matrix with $H^+$) or ATP/ADP exchange. Depolarization of the MIM was observed by other authors using cationic dyes [9,11].

On the other hand, important differences were observed in the spare respiratory capacity. This index was unchanged for stress-induced ($H_2O_2$, doxorubicin) and replicative senescent cells, but increased more than 50% in RAS-induced senescent cells (Table 1). These results are in agreement with the increase in mtDNA/nDNA and mitochondrial mass in OIS [9,10] and indicate that senescent cells can efficiently respond to energy demands or damaging insults [34]. Moreover, recent results by Victorelli et al. show that senescent cells release mtDNA as part of the signals triggering the SASP [16], pointing towards a possible alternative role of these "spare" mitochondria in inflammatory signaling rather than bioenergetics. The increase in mitochondrial reactive oxy-gen species formation observed in senescent cells [9,23] could also play a role in signaling events, maintaining a persistent activation of the DDR or affecting chromatin remodeling and gene expression [63,64].

Finally, we compared the respiratory control ratio (RCR) of senes-cent cells induced by different stimuli. The RCR is considered a good marker of mitochondrial bioenergetic dysfunction, since it considers both the maximum activity of the respiratory chain and the existence of uncoupling events [34]. The RCR was higher in control than in senescent cells induced by $H_2O_2$, doxorubicin or serial passage (relicative senes-cence) (Table 1) in agreement with mitochondrial bioenergetic dysfunction. Instead, a significant increase in the RCR was observed in oncogene-induced senescent cells, supporting an overall improvement of mitochondrial bioenergetics (Table 1).

Mitochondrial fatty-acid oxidation increased in OIS but not in doxorubicin- or $H_2O_2$-induced senescence. In agreement, inhibition of ACC by phosphorylation in serine 79 by AMPK was only observed in the presence of the oncogene.

AMPK phosphorylation in OIS was first reported by Moiseeva et al., along with a 40% decrease in ATP levels in senescent with respect to control cells [9]. At the time this was interpreted as evidence of mito-chondrial dysfunction, however, functional analysis measuring oxygen consumption rates reported here (Figs. 2–4) and previously [12,13,26] show that mitochondrial respiration and oxidative phosphorylation are highly active routes in OIS. These results suggest that low levels of ATP might be due to an increase in ATP hydrolysis rather than a decrease in ADP phosphorylation. Protein synthesis and secretion are energy demanding processes [65], and probably responsible for the changes in ATP/ADP or ATP/AMP ratios that activate AMPK [66]. Upon activation AMPK phosphorylates several factors, inhibiting anabolic pathways, activating catabolic pathways (e.g. fatty acid oxidation, glycolysis), and promoting PGC-1α-dependent mitochondrial biogenesis [66]. Overall these events lead to a long-term increase in cell respiration and adap-tation to the energy demands imposed by the SASP. In fact, inhibition of AMPK with CC reduced both oxygen consumption rates and cytokine secretion in OIS (Fig. 6).

In sum, reports of increased mitochondrial reactive oxygen species and mitochondrial mass, lower mitochondrial membrane potential, and release of mtDNA and mtRNA to the cytoplasm have been considered signals of mitochondrial dysfunction in senescence [9,11]. However, when it comes to mitochondrial bioenergetics our results indicate the metabolic phenotype depends on the inducing stimuli, as happens for the DDR, the SASP and the expression of multiple genes [6].

The increase in respiratory rates along with the analysis of metabo-lites and enzymes suggest that in OIS, acetyl-CoA is generated during
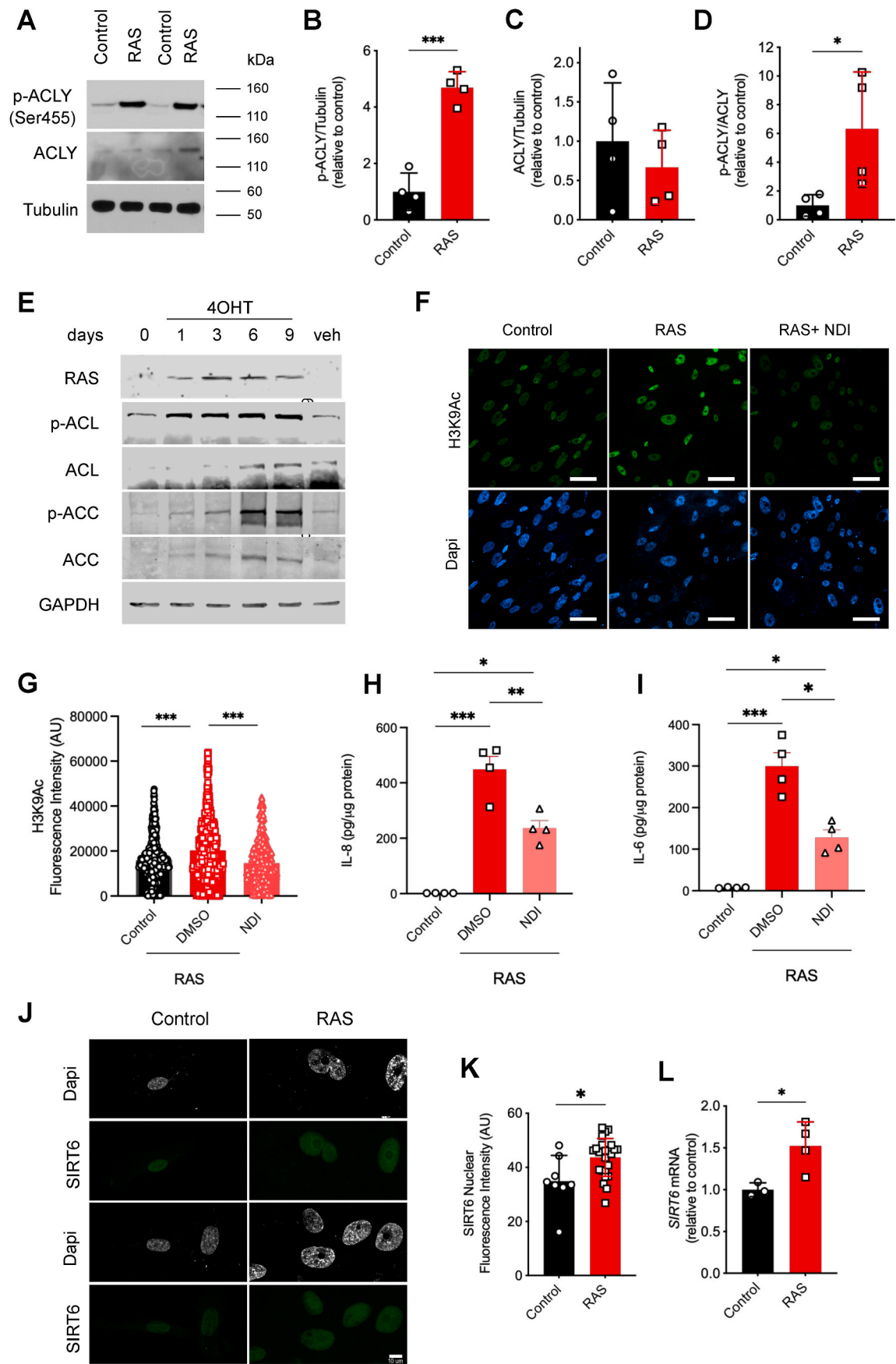
**Fig. 8. ACLY-dependent histone lysine acetylation in oncogene-induced senescent cells. (A–D)** Early passage IMR-90 human fibroblasts expressing the H-RAS$^{G12V}$ oncogene (RAS) or a control plasmid (Control). **(A)** Representative WB for ACLY and phosphorylated ACLY (p-ACLY) (Ser455) and tubulin as loading control. **(B–D)** Quantification of ACLY and p-ACLY relative to tubulin and the ratio between the phosphorylated and total enzyme, normalized to the control condition. **(E)** WB of BJERRAS fibroblasts at different time points after the addition of 4OHT (200 nM) or the vehicle showing an increase in RAS, p-ACLY, ACLY, p-ACC, ACC and GAPDH as loading control. **(F–I)** OIS IMR-90 fibroblasts treated with the ACLY inhibitor NDI-091143 (NDI, 40 μM) for 18 h or the vehicle: **(F)** Histone acetylation measured by confocal microscopy after immunocytochemistry using anti-H3K9Ac antibody (green) and staining the nuclei with Dapi (blue). **(G)** Quantification of nuclear H3K9Ac (n > 300). **(H and I)** Secretion of IL-8 and IL-6 measured by ELISA (n = 4). **(J)** SIRT6 levles obtained by confocal microscopy after immunocytochemistry with an anti-SIRT6 antibody (green), and nuclei stained with Dapi (white). **(J)** Quantification of nuclear SIRT6 (n = 8–25). **(K)** Expression levels of *SIRT6* determined by RT-qPCR (n = 3–4). Significant differences between conditions were determined with Student's t-test or one-way ANOVA and Tukey post-hoc for multiple comparisons *P < 0.05, **P < 0.001, ***P ≤ 0.0001.

oxidation of fatty acids and glucose, and pyruvate oxidative decarboxylation by PDH. Acetyl-CoA can condense with oxaloacetate forming citrate and is oxidized completely in the TCA cycle resulting in increased respiration rates and ATP synthesis. However, partial inhibition of aconitase along with increased ACLY phosphorylation (Ser455), that results in enzyme activation, points to a possible export of citrate leading to a re-distribution of the sub-cellular acetyl-CoA pools. Interestingly, Nacarelli et al. [27] have also observed an increase in glycolytic intermediates, along with high levels of acetyl-CoA and citrate in OIS.

In proliferating cells citrate shuttle from mitochondria to cytoplasm is mostly associated with fatty acid synthesis. Yet, in senescent cells where ACC is phosphorylated by AMPK and lipid synthesis inhibited acetyl-CoA can be diverted to towards acetylation of protein lysine residues in histones or other targets. Acetylation is a relevant post-translational modification that regulates multiple metabolic pathways, as well as gene expression [67]. Of special interest in the context of senescence is the reported role of ACLY in DNA damage repair [50]. ATM activation promotes ACLY phosphorylation by Akt [50], and can also activate AMPK [68], redirecting acetyl-CoA from lipid synthesis towards histone acetylation upon DNA damage. Our results reveal ACLY phosphorylation increases in OIS and its activity is required for H3K9 acetylation (Fig. 8). Acetylated histone H3K9 accumulates in promoter regions of IL-6 and IL-8 and has been shown to promote their expression [69]. Accordingly here we show that pharmacological inhibition of ACLY reduces the secretion of these proinflammatory cytokines in OIS (Fig. 8). Epigenetic alterations regulate the expression of multiple SASP components [70] and our results support a role for metabolic pathways in these processes. Other interesting observations that merit further study are the changes in TCA cycle metabolite levels. In particular, the decrease in α-ketoglutarate and increase in succinate and fumarate in OIS (Fig. 7) could inhibit α-ketoglutarate-dependent dioxygenases. These enzymes are involved in proline hydroxylation and stabilization of transcription factor HIF and chromatin demethylation, and can influence cell metabolism and gene expression [71]. Interestingly, the decrease in α-ketoglutarate could be due to superoxide-mediated aconitase inactivation, pointing to a potential role for this reactive oxygen species regulating the abundance of epigenetically active metabolites [22]. Nevertheless, we must mention that a recent report by Tighanimine et al. shows an increase in α-ketoglutarate and α-ketoglutarate/succinate ratios in OIS fibroblasts when compared to non-senescent cells [17]. Differences between this report and the data presented herein might be due to the cell lines used in the assays (WI-38 fibroblasts vs IMR-90); or alternatively to non-senescent cells being in a proliferative or a quiescent state, respectively, since α-ketoglutarate and succinate levels have been shown to differ in these conditions [72].

Finally, assessment of SIRT6, a NAD$^{+}$-dependent deacetylase, showed an important increase in gene expression, in agreement with previous transcriptomic analysis [73]. SIRT6 protein levles were also increased and localized in the nuclei of oncogene-induced senescent cells. Long chain free fatty acids can increase SIRT6 catalytic activity [74], and these lipids are higher in senescent than control fibroblasts [13]. SIRT6 catalyzes de deacetylation of histone H3K9 in the promoter region of multiple genes involved in glucose and fatty acid metabolism, favoring oxidative metabolism over glucose fermentation and lipid synthesis [57–60]. SIRT6 also promotes phosphorylation (Thr172) and

activation of AMPK, as well as mitochondrial respiration and oxidative phosphorylation [59]. In addition, this sirtuin can sense DNA damage and activate the DDR [56]. Several reports indicate that SIRT6 impacts on NF-κB activity, and both pro- and anti-inflammatory roles have been described [61]. Thus, this multitasking enzyme could coordinately regulate DNA damage repair, nutrient catabolism and the proinflammatory SASP in senescent cells. SIRT6 can also consume NAD$^{+}$, and several reports argue that NAD$^{+}$/NADH ratios play a relevant role regulating AMPK activation and the SASP [27,31], but the role of this cofactor in senescence is complex and requires further exploration [75].

## 4. Conclusions

The prominent role of mitochondria sustaining the SASP highlights the relevance of studying its physiology and regulation in senescence. Overall, our work supports the existence of catabolic heterogeneity among senescent cells, showing that hydrogen peroxide, doxorubicin and replicative senescent cells present a decrease in mitochondrial bioenergetics; while oncogene-induced senescent fibroblasts have an overall increase in mitochondrial energy metabolism pathways that depends on the continuous expression of the oncogene and activation of AMPK. Besides, we provide a detailed description of mitochondrial energy metabolism (Fig. 9) and identify new features of metabolic pathways in OIS cells, such as an increase in PDH and ACLY phosphorylation and inactivation of aconitase, that could affect the fate of acetyl-CoA moieties. Moreover, we show that AMPK and ACLY regulate the metabolic phenotype and drive the SASP in OIS.

## 5. Materials and methods

### 5.1. Doxorubicin and $H_2O_2$ induced senescence in fibroblasts

IMR-90 (ATCC® CCL-186) human lung fibroblasts were obtained from ATCC (Manassas, Virginia, USA) with 10 passages in culture and at a population doubling level (PDL) of 25. Fibroblasts were routinely grown in Dulbecco's modified Eagle's medium (DMEM, Invitrogen) supplemented with 10% (v/v) fetal bovine serum (FBS), penicillin 50 U/ml and streptomycin 50 μg/ml (complete media). Cells were maintained at 37 °C in a CO$_2$ incubator (95 % air, 5 % CO$_2$). Under our experimental conditions, IMR-90 cultures entered senescence after achieving a PDL value of 50 obtained after 22–24 passages. Cells between passage 10–18, early passage cells (PDL 25–36), were used in all the experiments unless otherwise specified.

For doxorubicin (Sigma) treatment cells were seeded at 1-4 × 10$^4$ cell/cm$^2$, three days after plating cells were incubated with 0.2 μM doxorubicin, for the indicated periods.

For H$_2$O$_2$ treatment cells were seeded at 1-4 × 10$^4$ cell/cm$^2$ and 24 h later exposed for 2 h to 600 μM H$_2$O$_2$ in complete media. Four days after the first treatment the cells were split 1:3 and treated again for 2 h with 600 μM H$_2$O$_2$. Hydrogen peroxide was quantified spectrophotometrically ($\varepsilon_{240} = 43.6$ M$^{-1}$ cm$^{-1}$).

### 5.2. Oncogene-induced senescence

The lentiviral plasmid expressing H-RAS containing a glycine to

## Mitochondrial energy metabolism in OIS
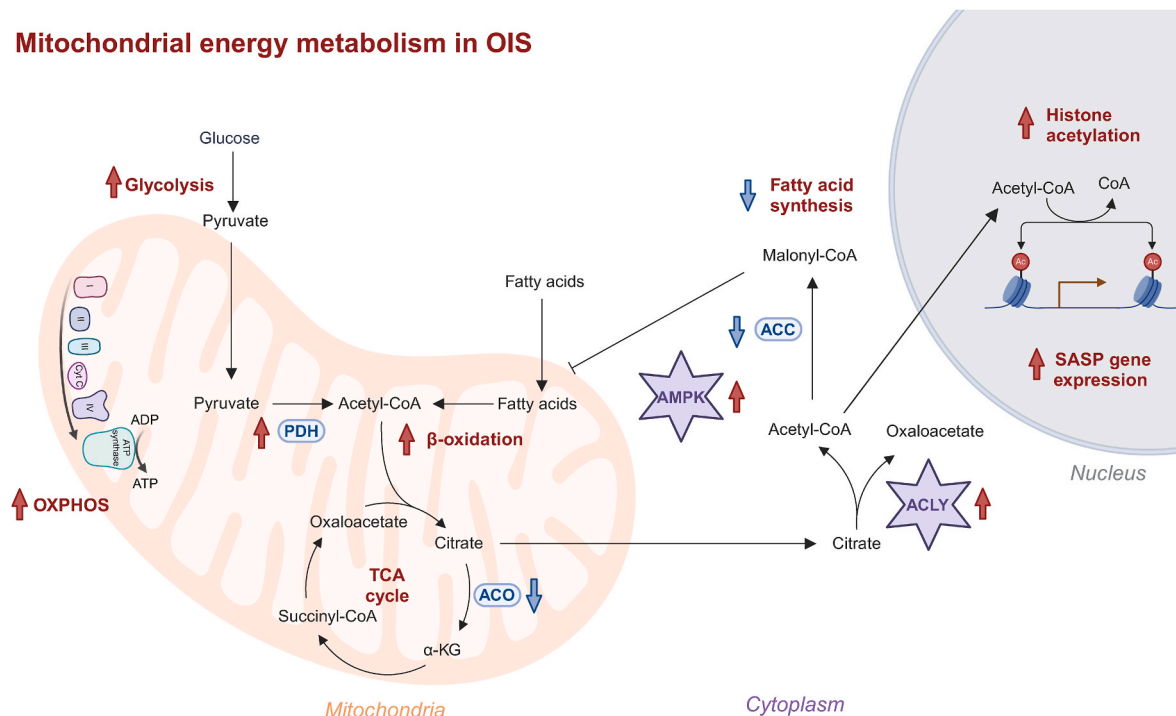


**Fig. 9. Mitochondrial energy metabolism and metabolic fates of acetyl-CoA in OIS cells.** Glucose and fatty-acid oxidation increase in OIS resulting in the formation of acetyl-CoA. Acetyl-CoA condenses with oxaloacetate forming citrate, that can be oxidized in the TCA cycle or exported to the cytoplasm, and regenerate acetyl-CoA. Since lipid synthesis is inhibited in these cells, acetyl-CoA can be rerouted and participate in protein lysine acetylation, promoting histone acetylation and SASP gene expression. AMPK and ACLY activation play key roles regulating metabolic reactions and the SASP. Enzymes and pathways where evidence of an increase or decrease in activity was found are shown with a red arrow or a blue arrow, respectively. ACC: acetyl-CoA carboxylase; ACLY: ATP-citrate lyase; ACO: mitochondrial aconitase; AMPK: AMP activated protein kinase; PDH: pyruvate dehydrogenase complex. The figure was created with BioRender.com.

valine substitution at position 12 (H-RAS$^{G12V}$, oncogene RAS) was a gift from Eric Campeau (pLenti CMV/TO RasV12 Puro (w119-1), Addgene plasmid #22262). The control plasmid pLKO.1 was from Open Biosystems. Plasmids pCMV-dR8.2 dvpr and pCMV-VSVG were a gift from Bob Weinberg (Addgene plasmids #8455 and #8454, respectively) [76]. Lentiviral constructs were amplified in 293T cells according to protocols established by the Broad Institute RNAi Consortium [77].

Early passage IMR-90 cells were transduced with lentiviruses (MOI of 1–5) overnight in media containing 8 μg/ml polybrene, one to two days after seeding. Transduced cells were subsequently selected in culture media supplemented with 2 μg/ml puromycin (Sigma-Aldrich). Unless otherwise specified, all experiments regarding RAS-induced senescence were performed 14 days after transduction [13].

Alternatively skin fibroblasts (BJ) carrying the H-RAS$^{G12V}$ oncogene fused to the ligand binding domain of the estrogen receptor (ERRAS) were generated with pLNCX2 ER:Ras (Addgene plasmid #67844) [78] as described [79]. Cutaneous fibroblasts carrying ERRAS were cultured as described above and RAS expression induced incubating with 200 nM 4-hydroxytamoxifen (4OHT), media with 4OHT was replenished every 2–3 days during the experiment [79]. Samples were collected and processed at the indicated time points.

Senescent and control cells were incubated with the AMPK inhibitor compound C (CC, Selleckchem) also known as dorsomorphin, the ACLY inhibitor NDI-091143 (NDI, Selleckchem) in conditions previously described in the literature [39,51,52,80].

### 5.3. Replicative senescence

IMR-90 human lung fibroblasts, at a population doubling level (PDL) of 25, were subcultured weekly using an initial seeding density of 0.5 × $10^6$ cells per 10 cm dish. Cells between passage 10–18 were denominated early passage cells (PDL 25–36). IMR-90 cultures entered

replicative senescence after achieving a PDL value of 50 obtained after 22–24 passages. At this point, fibroblasts could not reach confluence after 7–10 days following a 1:2 split and 60–80 % cells stained positive for SA-β-Gal [32].

### 5.4. Western blots

Cells were routinely lysed in cell lysis buffer containing 20 mM Tris-HCl, pH 7.5, 1 % Triton X-100, 150 mM NaCl, 1 mM EDTA, 1 mM EGTA, 2.5 mM sodium pyrophosphate, 1 mM β-glycerophosphate, 1 mM Na$_2$VO$_4$, supplemented with protease (Sigma FAST) and phosphatase inhibitor (Calbiochem) cocktails. Lysates were sonicated, centrifuged at 14000 g for 10 min and stored at −80 °C. Proteins (20–40 μg) were resolved by SDS-PAGE and subjected to western blotting using standard procedures.

The following primary antibodies and dilutions were used: ACO (#ab71440, 1:1000), MFN1 (#ab104274, 1:4000), MFN2 (#ab124773, 1:5000), pyruvate dehydrogenase (PDH) antibody cocktail (#ab110416, 1:250), succinate dehydrogenase (SDH) subunit A (#ab14715, 1:1000), β-tubulin (#ab6046, 1:1000) and α-actin (#ab5694, 1:1000) from Abcam; RAS (#3339, 1:1000), ACC (#3676, 1:1000) according to the provider this antibody recognizes the two isoforms ACC1(265 kDa) and ACC2 (280 kDa), phospho-ACC (Ser79) (#3661, 1:1000) according to the provider this antibody recognizes the two phosphorylated isoforms ACC1 in Ser79 and ACC2 in the equivalent residue (Ser219), acetylated-lysine (#9441, 1:1000), ACLY (#4332, 1:1000), phospho-ACLY (Ser455) (#4331, 1:1000) AMPK (#2532, 1:1000), phospho-AMPK (Thr172) (#2535, 1:1000), ATM (#2873, 1:1000), ERK (#4695, 1:1000), phospho-ERK (Thr202/Tyr204) (#4370, 1:1000), phospho-p53 (Ser15) (#9284, 1:1000), p21 (#2947), SIRT1 (#8469, 1:1000), SIRT3 (#5409, 1:1000), SIRT6 (#12486, 1:1000), p65 (#8242, 1:1000) and GAPDH (#2118, 1:1000) from Cell Signaling Technology; phospho-

ATM (Ser1981) (#05–740, 1:1000) from Millipore; phospho-pRb (Ser807/Ser811) (#558389, 1:10000) from BD Pharmingen; p16 (#468, 1:1000), p53 (DO-1, sc-126, 1:250), p53 (sc-6243, 1:1000), p21 (sc-6246, 1:1000) and α-tubulin (sc-8035, 1:500) from Santa Cruz Biotechnology. Western blots were analyzed with Image Studio Lite (LI-COR Bioscience) or ImageJ.

### 5.5. Immunocytochemistry

For SIRT6 analysis cells were cultured in permanox chamber slides (Thermo Fisher Scientific) fixed in 4% paraformaldehyde, permeabilized with 0.2% Triton in PBS, incubated in blocking buffer (3% BSA, 0.2% Triton in PBS) for 1 h and incubated with primary antibody anti SIRT6 (#12486, 1:50) or from Cell Signaling Technology overnight at 4 °C. The following day cells were incubated with the secondary antibody Alexa Fluor® 488 goat anti-rabbit IgG (H + L) (#A11034) from Thermo Fisher Scientific for 1 h at room temperature and 4,6-diamidino-2-phenylindole (Dapi, 1 mg/ml, Thermo Fisher Scientific) was used to stain the nuclei. Labeled proteins were visualized using a confocal microscope (Leica, SP5) and image analysis was performed in ImageJ.

For H3K9Ac analysis cells were cultured in glass coverslips coated with 0.2% gelatin, fixed in 4% paraformaldehyde permeabilized with 0.3% Triton in PBS, incubated in blocking buffer (10% normal goat serum, 0.3% Triton, in PBS) for 1 h and incubated with primary antibody anti- H3K9Ac (#9649, 1:400) from Cell Signaling Technology overnight at 4 °C. Cells were then incubated with the secondary antibody (anti-rabbit AF488 1:1000, Invitrogen) and Dapi. Image acquisition was performed using a Carl Zeiss LSM 800, and images analyzed using Fiji.

For p16-INK4 analysis cells were cultured in glass coverslips coated with 0.2% gelatin, fixed in 4% paraformaldehyde, blocked and permeabilized with 3% BSA, 2% glycine, 0.3% Triton X-100 in PBS for 1 h and incubated with primary antibody anti-CDKN2A/p16-INK4a (#ab54210, 1:100) from Abcam overnight at 4 °C. Cells were then incubated with the secondary antibody (anti-rabbit antimouse Alexa-Fluor 488 (#A-11094, 1:1000) from ThermoFisher and Dapi. Image acquisition was performed using a Nikon Eclipse TE-200, and images analyzed using ImageJ.

### 5.6. Gene expression analysis

Cells were homogenized in TRIzol (Thermo Fisher Scientific) following the manufacturer's recommendations and instructions. A DNase treatment was performed to eliminate possible contamination with genomic DNA (Roche, Cat. No. 04716728001). Complementary DNA was generated using Superscript II enzyme (Invitrogen, Cat. No. 18064-014). Quantitative real-time PCR was performed with Quanti-Tect® SYBR® Green PCR Kit (Qiagen) with specific primers. The relative changes in gene expression were expressed relative to the control with the $2^{-\Delta\Delta CT}$ method [81]. The following primers were used:

The relative changes in gene expression were expressed relative to the control as $2^{-\Delta CTcondition}/2^{-\Delta CTcontrol}$ method.

SIRT6: forward 5'-ACTGGCGAGGCTGGTCTG-3'
reverse 5'- GCTCTCAAAGGTGGTGTCG-3'
β-actin: forward 5'-AGCCATGTACGTAGCCATCC-3'
reverse 5'-GCTGTGGTGGTGAAGCTGTA-3'
LMNB1: forward 5'-GTATGAAGAGGAGATTAACGAGAC-3'
reverse 5'-TACTCAATTTGACGCCCAG-3'
CDKN2A: forward 5'-ATCATCAGTCACCGAAGGTC-3'
reverse 5'-CTCAAGAGAAGCCAGTAACC-3'

### 5.7. Mitochondrial oxygen consumption rate

Oxygen consumption rate (OCR) was measured in a Seahorse XFe24 extracellular flux analyzer (Agilent). Before the experiment, the culture medium was replaced with an unbuffered medium: DMEM (D5030, Sigma) pH 7.4, supplemented with 32 mM NaCl, 5 mM glucose, 1 mM

sodium pyruvate and 2 mM glutamine. Cells were incubated for 1 h at 37 °C in a stove without $CO_2$. Basal oxygen consumption measurements were taken before the injection of oxidative phosphorylation inhibitors or an uncoupler. For mitochondrial respiratory analysis, successive measurements were taken after the sequential addition of oligomycin (0.5 μM), carbonyl cyanide 4-(trifluoromethoxy)phenylhydrazone (FCCP, 1 μM one or two additions) and antimycin A (AA, 1 μM). After each assay, protein content (μg) per well was determined with the bicinchoninic acid (BCA) technique (Pierce, Thermo Scientific) and OCR were normalized considering protein content (mg) or cell number. Antimycin A-resistant respiration (non-mitochondrial respiration) was subtracted from all oxygen consumption measurements [34].

Basal respiration was determined in the absence of mitochondrial inhibitors and represents the sum of all mitochondrial oxygen-consuming processes. ATP-independent respiration (also known as proton leak) was the OCR resistant to the addition of ATP synthase inhibitor oligomycin. ATP-dependent respiration was calculated as the difference between basal and ATP-independent respiration. The maximum respiration rate, was obtained after titration with the mitochondrial uncoupler FCCP.

Respiratory indexes were determined as ratios between the respiratory rates The coupling efficiency was the ratio between ATP-dependent and basal respiration. Spare respiratory capacity was the ratio between the maximum and basal respiration rates. Finally, the respiratory control ratio (RCR) was the ratio between maximum and ATP-independent rates.

Alternatively, we used the Resipher real time cell analyzer (Lucid) to measure basal oxygen consumption rates in real time and continuously through the induction and establishment of senescence. Complete media was changed every two to three days and measurement were performed at 37 °C in a $CO_2$ incubator (95 % air, 5 % $CO_2$). At the end of the experiment protein content (μg) per well was determined with BCA (Pierce, Thermo Scientific) and OCR were normalized considering protein content.

### 5.8. Fatty acid oxidation

Fatty acid oxidation was measured assessing oxygen consumption rate (OCR) in the presence of oleate conjugated to BSA (OA-BSA), OA: BSA 0.1 mM:0.2% m/v, in the XFe24 extracellular flux analyzer (Agilent). Briefly, cells were initially changed to unbuffered DMEM (DMEM with 5 mM glucose, 1 mM sodium pyruvate, 32 mM NaCl, 2 mM glutamine, pH 7.4), and incubated in a non-$CO_2$ incubator for 2 h at 37 °C. OA-BSA was added to the medium and four baseline measurements were taken before injecting etomoxir (100 μM) and antimycin A (2.5 μM) [13].

Fatty acid conjugation. To conjugate the free fatty acid oleate to BSA, we initially prepared 100 mM sodium oleate (Sigma- Aldrich) by mixing 47.5 mg of oleate in 1.5 ml of water with 2.5 μl of 1 N NaOH. The solution was heated to 37 °C and vortexed occasionally until dissolved. Sodium oleate was then mixed with a solution of fatty acid free BSA (Sigma) dissolved in PBS (15% weight to volume). The resulting mixture was then incubated for 30 min at 42 °C to obtain an oleate:BSA stock solution (7 mM:14%) [13].

### 5.9. Aconitase activity

Subcellular fractions were obtained according to [82]. Two culture dishes (140 mm diameter) of IMR-90 fibroblasts were used per condition. Cells were washed with cold PBS, scraped and resuspended in fractionation buffer (FB: 0.25 M sucrose, 10 mM Tris-HCl, 0.1 mM EDTA, 2 mM sodium citrate, and 1 mM sodium succinate), and homogenized using a Potter-Elvehjem. The homogenate was centrifuged at 1500 g for 10 min to eliminate the nuclei and remaining cells. The supernatant was centrifuged at 13000 g for 10 min to obtain fractions enriched in cytoplasm and mitochondria. The pellet, containing the

enriched mitochondrial fraction, was resuspended in 200 μl of FB with 1 % Triton X-100.

Aconitase activity was assayed immediately in cytoplasm and mitochondria enriched fractions measuring *cis*-aconitate at 240 nm ($\varepsilon_{240nm}$ = 3.6 mM$^{-1}$ cm$^{-1}$) (Shimadzu UV-2450), after the addition of 8 mM isocitrate in 100 mM Tris-HCl buffer, pH 7.8. The assays were carried out in the absence or presence of the enzyme inhibitor fluorocitrate (35 μM), to discriminate the increase in absorbance caused by the reaction under study from those due to other reactions that could be taking place in parallel [83].

Aconitase reactivation was achieved incubating with 10 mM dithiothreitol (DTT) and 100 μM Fe(NH$_4$)$_2$(SO$_4$)$_2$ under argon for 30 min in an anaerobic vial [84].

Since aconitase is selectively sensitive to superoxide O$_2^{\bullet-}$ the ratio between inactive and active mitochondrial aconitase (ACO2) was used to compare mitochondrial O$_2^{\bullet-}$ steady state levels in control and OIS cells. As described in the following equation:

$$\frac{\left[O_2^{\bullet-}\right]_{RAS}}{\left[O_2^{\bullet-}\right]_{Ctrl}} = \frac{([Inactive\ ACO2]/[Active\ ACO2])_{RAS}}{([Inactive\ ACO2]/[Active\ ACO2])_{Ctrl}}$$

The ratio between inactive and active enzyme in control cells was calculated considering that in normal (air) cultured cells a 10% inhibition of mitochondrial aconitase was observed by Gardner and White [85]. While in OIS cells the ratio was determined considering enzyme activity before and after reactivation [84].

### 5.10. Chloromethyl -2′,7′-dichlorodihydrofluorescein diacetate oxidation

Senescent and non-senescent fibroblasts were incubated with the cell-permeant probe chloromethyl-2′,7′- dichlorodihydrofluorescein diacetate (CM-H$_2$DCFDA, Invitrogen #6827) 5 μM for 30 min at 37 °C. Cells were then trypsinized and the fluorescence of chloromethyl-2′,7′-dichlorofluorescein (CM-DCF) was measured by flow cytometry using a LSRII instrument (Becton-Dickinson) [86].

DCFH-DA is a widely used probe for detecting intracellular oxidants. The acetyl moieties of the probe are hydrolyzed by intracellular esterases, producing chloromethyl-2′,7′- dichlorodihydrofluorescein (CM-H$_2$DCF), that can be oxidized by strong intracellular oxidants forming CM-DCF [87].

### 5.11. mtDNA/nDNA ratio

Cells were incubated in buffer 10 mM Tris, 10 mM EDTA, 100 mM NaCl, 0.5 % SDS and 0.5 mg/ml proteinase K for 1 h at 60 °C. For protein precipitation NaCl was added at 2 M final concentration followed by Phenol:Chloroform:Isoamyl alcohol (25:24:1, v/v) (Invitrogen #15593031). Total DNA precipitation was achieved with 100 % ethanol. DNA was quantified by measuring the absorbance at 260 nm and the purity of the samples was checked by calculating the A260/A280 ratio measured on a Scanning Micro-Volume Spectrophotometer (Janeway 7415). Separate tubes, with 20 ng of total DNA, were used for the amplification of mtDNA and nDNA. Quantitative RT-PCRs were carried out with PowerUp SYBR Green master mix and 0.5 μM of each primer. The measurements were performed on the Corbett Rotor-Gene 6000 (Thermo Fisher Scientific). The ratio of mtDNA to nDNA was calculated with the 2$^{-\Delta\Delta CT}$ method and the results were expressed relative to the control condition. The following primers were used.

18S rRNA (nuclear): forward 5'-CGCGGTTCTATTTTGTTGGT-3'

reverse 5'-AGTCGGCATCGTTTATGGTC-3'

MT-ND4L (mitochondrial): forward 5'-CACCCACTCCCTCTTAGC-CAAT-3'

reverse 5'-GGCCATATGTGTTGGAGATTGAGAC3'

### 5.12. Cytokine secretion

Cells were seeded in six-wells plates and three days after TMZ treatment cells were washed with PBS and added 1 ml of DMEM. Two days after the medium was collected, centrifuged at 1000g to remove cells and debris and stored at −80 °C. IL-6, IL-8, GRO-α, GM-CSF and MIP-1- α (CCL3) were assessed by ELISA using DuoSet ELISA kits (R&D Systems) or ELISA MAX™ Deluxe Set (BioLegend, BD Bioscience). Results were normalized to μg of protein or cell number.

### 5.13. Statistical analysis and graphs

All plots and statistical analysis were performed using GraphPad Prism. Data were analyzed by two-tailed unpaired Student's t-test (when comparing two groups); or one- or two-way ANOVA with Tukey or Dunnett's post hoc tests, as appropriate, (when comparing more than two groups). P < 0.05 was considered statistically significant. In all cases, results in the text show mean ± S.D. In all experiments, n values represent the number of independent biological samples (wells or culture dishes per group/condition). All experiments and statistical analysis were performed with n ≥ 3.

### CRediT authorship contribution statement

**Inés Marmisolle:** Writing – review & editing, Investigation, Funding acquisition, Formal analysis, Conceptualization. **Eliana Chacón:** Investigation. **Santiago Mansilla:** Investigation. **Santiago Ruiz:** Investigation, Formal analysis. **Mariana Bresque:** Investigation, Formal analysis. **Jennyfer Martínez:** Investigation, Formal analysis. **Ricardo Iván Martínez-Zamudio:** Methodology, Investigation. **Utz Herbig:** Supervision, Methodology. **Jie Liu:** Methodology, Investigation. **Toren Finkel:** Writing – review & editing, Conceptualization. **Carlos Escande:** Supervision, Funding acquisition, Conceptualization. **Laura Castro:** Writing – review & editing, Supervision, Funding acquisition, Conceptualization. **Celia Quijano:** Writing – review & editing, Writing – original draft, Supervision, Project administration, Investigation, Funding acquisition, Formal analysis, Data curation, Conceptualization.

### Funding

### Declaration of competing interest

None.

### Acknowledgements

## Appendix A. Supplementary data

Supplementary data to this article can be found online at https://doi.org/10.1016/j.redox.2025.103606.

## Data availability

Data will be made available on request.

## References

[1] V. Gorgoulis, P.D. Adams, A. Alimonti, D.C. Bennett, O. Bischof, C. Bishop, J. Campisi, M. Collado, K. Evangelou, G. Ferbeyre, J. Gil, E. Hara, V. Krizhanovsky, D. Jurk, A.B. Maier, M. Narita, L. Niedernhofer, J.F. Passos, P.D. Robbins, C. A. Schmitt, J. Sedivy, K. Vougas, T. Von Zglinicki, D. Zhou, M. Serrano, M. Demaria, Cellular senescence: defining a path forward, Cell 179 (2019) 813–827, https://doi.org/10.1016/j.cell.2019.10.005.

[2] V. Suryadevara, A.D. Hudgins, A. Rajesh, A. Pappalardo, A. Karpova, A.K. Dey, A. Hertzel, A. Agudelo, A. Rocha, B. Soygur, B. Schilling, C.M. Carver, C. Aguayo-Mazzucato, D.J. Baker, D.A. Bernlohr, D. Jurk, D.B. Mangarova, E.M. Quardokus, E.A.L. Enninga, E.L. Schmidt, F. Chen, F.E. Duncan, F. Cambuli, G. Kaur, G. A. Kuchel, G. Lee, H.E. Daldrup-Link, H. Martini, H. Phatnani, I.M. Al-Naggar, I. Rahman, J. Nie, J.F. Passos, J.C. Silverstein, J. Campisi, J. Wang, K. Iwasaki, K. Barbosa, K. Metis, K. Nernekli, L.J. Niedernhofer, L. Ding, L. Wang, L.C. Adams, L. Ruiyang, M.L. Doolittle, M.G. Teneche, M.J. Schafer, M. Xu, M. Hajipour, M. Boroumand, N. Basisty, N. Sloan, N. Slavov, O. Kuksenko, P. Robson, P. T. Gomez, P. Vasilikos, P.D. Adams, P. Carapeto, Q. Zhu, R. Ramasamy, R. Perez-Lorenzo, R. Fan, R. Dong, R.R. Montgomery, S. Shaikh, S. Vickovic, S. Yin, S. Kang, S. Suvakov, S. Khosla, V.D. Garovic, V. Menon, Y. Xu, Y. Song, Y. Suh, Z. Dou, N. Neretti, SenNet recommendations for detecting senescent cells in different tissues, Nat. Rev. Mol. Cell Biol. (2024), https://doi.org/10.1038/s41580-024-00738-8.

[3] R. Yosef, N. Pilpel, R. Tokarsky-Amiel, A. Biran, Y. Ovadya, S. Cohen, E. Vadai, L. Dassa, E. Shahar, R. Condiotti, I. Ben-Porath, V. Krizhanovsky, Directed elimination of senescent cells by inhibition of BCL-W and BCL-XL, Nat. Commun. 7 (2016) 11190, https://doi.org/10.1038/ncomms11190.

[4] A. Hernandez-Segura, J. Nehme, M. Demaria, Hallmarks of cellular senescence, Trends Cell Biol. 28 (2018) 436–453, https://doi.org/10.1016/j.tcb.2018.02.001.

[5] G.P. Dimri, X. Lee, G. Basile, M. Acosta, G. Scott, C. Roskelley, E.E. Medrano, M. Linskens, I. Rubelj, O. Pereira-Smith, et al., A biomarker that identifies senescent human cells in culture and in aging skin in vivo, Proc. Natl. Acad. Sci. U. S. A. 92 (1995) 9363–9367.

[6] A. Hernandez-Segura, T.V. De Jong, S. Melov, V. Guryev, J. Campisi, M. Demaria, Unmasking transcriptional heterogeneity in senescent cells, Curr. Biol. 27 (2017) 2652–2660.e4, https://doi.org/10.1016/j.cub.2017.07.033.

[7] P.A. Perez-Mancera, A.R. Young, M. Narita, Inside and out: the activities of senescence in cancer, Nat. Rev. Cancer 14 (2014) 547–558, https://doi.org/10.1038/nrc3773.

[8] C.D. Wiley, J. Campisi, The metabolic roots of senescence: mechanisms and opportunities for intervention, Nat. Metab. 3 (2021) 1290–1301, https://doi.org/10.1038/s42255-021-00483-8.

[9] O. Moiseeva, V. Bourdeau, A. Roux, X. Deschênes-Simard, G. Ferbeyre, Mitochondrial dysfunction contributes to oncogene-induced senescence, Mol. Cell Biol. 29 (2009) 4495–4507.

[10] C. Correia-Melo, F.D. Marques, R. Anderson, G. Hewitt, R. Hewitt, J. Cole, B. M. Carroll, S. Miwa, J. Birch, A. Merz, M.D. Rushton, M. Charles, D. Jurk, S.W. Tait, R. Czapiewski, L. Greaves, G. Nelson, Y.M. Bohlooly, S. Rodriguez-Cuenca, A. Vidal-Puig, D. Mann, G. Saretzki, G. Quarato, D.R. Green, P.D. Adams, T. von Zglinicki, V.I. Korolchuk, J.F. Passos, Mitochondria are required for pro-ageing features of the senescent phenotype, EMBO J. 35 (2016) 724–742, https://doi.org/10.15252/embj.201592862.

[11] J.F. Passos, G. Saretzki, S. Ahmed, G. Nelson, T. Richter, H. Peters, I. Wappler, M. J. Birket, G. Harold, K. Schaeuble, M.A. Birch-Machin, T.B. Kirkwood, T. von Zglinicki, Mitochondrial dysfunction accounts for the stochastic heterogeneity in telomere-dependent senescence, PLoS Biol. 5 (2007) e110, https://doi.org/10.1371/journal.pbio.0050110.

[12] J. Kaplon, L. Zheng, K. Meissl, B. Chaneton, V.A. Selivanov, G. Mackay, S.H. van der Burg, E.M. Verdegaal, M. Cascante, T. Shlomi, A key role for mitochondrial gatekeeper pyruvate dehydrogenase in oncogene-induced senescence, Nature 498 (2013) 109–112.

[13] C. Quijano, L. Cao, M.M. Fergusson, H. Romero, J. Liu, S. Gutkind, I. Rovira, R. P. Mohney, E.D. Karoly, T. Finkel, Oncogene-induced senescence results in marked metabolic and bioenergetic alterations, Cell Cycle 11 (2012) 1383–1392, https://doi.org/10.4161/cc.19800.

[14] J. Martinez, D. Tarallo, L. Martinez-Palma, S. Victoria, M. Bresque, S. Rodriguez-Bottero, I. Marmisolle, C. Escande, P. Cassina, G. Casanova, M. Bollati-Fogolin, C. Agorio, M. Moreno, C. Quijano, Mitofusins modulate the increase in mitochondrial length, bioenergetics and secretory phenotype in therapy-induced senescent melanoma cells, Biochem. J. 476 (2019) 2463–2486, https://doi.org/10.1042/BCJ20190405.

[15] J.R. Dorr, Y. Yu, M. Milanovic, G. Beuster, C. Zasada, J.H. Dabritz, J. Lisec, D. Lenze, A. Gerhardt, K. Schleicher, S. Kratzat, B. Purfurst, S. Walenta, W. Mueller-Klieser, M. Graler, M. Hummel, U. Keller, A.K. Buck, B. Dorken, L. Willmitzer,

M. Reimann, S. Kempa, S. Lee, C.A. Schmitt, Synthetic lethal metabolic targeting of cellular senescence in cancer therapy, Nature 501 (2013) 421–425, https://doi.org/10.1038/nature12437.

[16] S. Victorelli, H. Salmonowicz, J. Chapman, H. Martini, M.G. Vizioli, J.S. Riley, C. Cloix, E. Hall-Younger, J. Machado Espindola-Netto, D. Jurk, A.B. Lagnado, L. Sales Gomez, J.N. Farr, D. Saul, R. Reed, G. Kelly, M. Eppard, L.C. Greaves, Z. Dou, N. Pirius, K. Szczepanowska, R.A. Porritt, H. Huang, T.Y. Huang, D. A. Mann, C.A. Masuda, S. Khosla, H. Dai, S.H. Kaufmann, E. Zacharioudakis, E. Gavathiotis, N.K. LeBrasseur, X. Lei, A.G. Sainz, V.I. Korolchuk, P.D. Adams, G. S. Shadel, S.W.G. Tait, J.F. Passos, Apoptotic stress causes mtDNA release during senescence and drives the SASP, Nature 622 (2023) 627–636, https://doi.org/10.1038/s41586-023-06621-4.

[17] K. Tighanimine, J.A. Nabuco Leva Ferreira Freitas, I. Nemazanyy, A. Bankolé, D. Benarroch-Popivker, S. Brodesser, G. Doré, L. Robinson, P. Benit, S. Ladraa, Y. B. Saada, B. Friguet, P. Bertolino, B. Canaud, P. Rustin, E. Gilson, O. Bischof, S. Fumagalli, M. Pende, A homeostatic switch causing glycerol-3-phosphate and phosphoethanolamine accumulation triggers senescence by rewiring lipid metabolism, Nat. Metab. 6 (2024) 323–342, https://doi.org/10.1038/s42255-023-00972-y.

[18] A.S. Monzel, J.A. Enríquez, M. Picard, Multifaceted mitochondria: moving mitochondrial science beyond function and dysfunction, Nat. Metab. 5 (2023) 546–562, https://doi.org/10.1038/s42255-023-00783-1.

[19] J. Nunnari, A. Suomalainen, Mitochondria: in sickness and in health, Cell 148 (2012) 1145–1159, https://doi.org/10.1016/j.cell.2012.02.035.

[20] J.X. Tan, T. Finkel, Mitochondria as intracellular signaling platforms in health and disease, JCB (J. Cell Biol.) 219 (2020) e202002179, https://doi.org/10.1083/jcb.202002179.

[21] M. Picard, O.S. Shirihai, Mitochondrial signal transduction, Cell Metab. 34 (2022) 1620–1653, https://doi.org/10.1016/j.cmet.2022.10.008.

[22] F.R. Palma, B.N. Gantner, M.J. Sakiyama, C. Kayzuka, S. Shukla, R. Lacchini, B. Cunniff, M.G. Bonini, ROS production by mitochondria: function or dysfunction? Oncogene 43 (2024) 295–303, https://doi.org/10.1038/s41388-023-02907-z.

[23] A.C. Lee, B.E. Fenster, H. Ito, K. Takeda, N.S. Bae, T. Hirai, Z.X. Yu, V.J. Ferrans, B. H. Howard, T. Finkel, Ras proteins induce senescence by altering the intracellular levels of reactive oxygen species, J. Biol. Chem. 274 (1999) 7936–7940.

[24] V. López-Polo, M. Maus, E. Zacharioudakis, M. Lafarga, C.S.-O. Attolini, F.D. M. Marques, E. Kovatcheva, E. Gavathiotis, M. Serrano, Release of mitochondrial dsRNA into the cytosol is a key driver of the inflammatory phenotype of senescent cells, Nat. Commun. 15 (2024) 7378, https://doi.org/10.1038/s41467-024-51363-0.

[25] K. Bartlett, S. Eaton, Mitochondrial β-oxidation, Eur. J. Biochem. 271 (2004) 462–469.

[26] S. Takebayashi, H. Tanaka, S. Hino, Y. Nakatsu, T. Igata, A. Sakamoto, M. Narita, M. Nakao, Retinoblastoma protein promotes oxidative phosphorylation through upregulation of glycolytic genes in oncogene-induced senescent cells, Aging Cell 14 (2015) 689–697, https://doi.org/10.1111/acel.12351.

[27] T. Nacarelli, L. Lau, T. Fukumoto, J. Zundell, N. Fatkhutdinov, S. Wu, K.M. Aird, O. Iwasaki, A.V. Kossenkov, D. Schultz, K.I. Noma, J.A. Baur, Z. Schug, H.Y. Tang, D.W. Speicher, G. David, R. Zhang, NAD(+) metabolism governs the proinflammatory senescence-associated secretome, Nat. Cell Biol. 21 (2019) 397–407, https://doi.org/10.1038/s41556-019-0287-4.

[28] M. Li, K.R. Durbin, S.M. Sweet, J.D. Tipton, Y. Zheng, N.L. Kelleher, Oncogene-induced cellular senescence elicits an anti-Warburg effect, Proteomics 13 (2013) 2585–2596, https://doi.org/10.1002/pmic.201200298.

[29] E. Hutter, K. Renner, G. Pfister, P. Stockl, P. Jansen-Durr, E. Gnaiger, Senescence-associated changes in respiration and oxidative phosphorylation in primary human fibroblasts, Biochem. J. 380 (2004) 919–928, https://doi.org/10.1042/BJ20040095.

[30] W. Zwerschke, S. Mazurek, P. Stockl, E. Hutter, E. Eigenbrodt, P. Jansen-Durr, Metabolic analysis of senescent human fibroblasts reveals a role for AMP in cellular senescence, Biochem. J. 376 (2003) 403–411, https://doi.org/10.1042/BJ20030816.

[31] C.D. Wiley, M.C. Velarde, P. Lecot, S. Liu, E.A. Sarnoski, A. Freund, K. Shirakawa, H.W. Lim, S.S. Davis, A. Ramanathan, A.A. Gerencser, E. Verdin, J. Campisi, Mitochondrial dysfunction induces senescence with a distinct secretory phenotype, Cell Metab. 23 (2016) 303–314, https://doi.org/10.1016/j.cmet.2015.11.011.

[32] I. Marmisolle, J. Martinez, J. Liu, M. Mastrogiovanni, M.M. Fergusson, I. Rovira, L. Castro, A. Trostchansky, M. Moreno, L. Cao, T. Finkel, C. Quijano, Reciprocal regulation of acetyl-CoA carboxylase 1 and senescence in human fibroblasts involves oxidant mediated p38 MAPK activation, Arch. Biochem. Biophys. 613 (2017) 12–22, https://doi.org/10.1016/j.abb.2016.10.016.

[33] J. Ngo, D.W. Choi, I.A. Stanley, L. Stiles, A.J.A. Molina, P. Chen, A. Lako, I.C. H. Sung, R. Goswami, M. Kim, N. Miller, S. Baghdasarian, D. Kim-Vasquez, A. E. Jones, N. Roach, V. Gutierrez, K. Erion, A.S. Divakaruni, M. Liesa, N.N. Danial, O.S. Shirihai, Mitochondrial morphology controls fatty acid utilization by changing CPT1 sensitivity to malonyl-CoA, EMBO J. 42 (2023) e111901, https://doi.org/10.15252/embj.2022111901.

[34] M.D. Brand, D.G. Nicholls, Assessing mitochondrial dysfunction in cells, Biochem. J. 435 (2011) 297–312, https://doi.org/10.1042/BJ20110162BJ20110162 [pii].

[35] S. Lee, C.A. Schmitt, The dynamic nature of senescence in cancer, Nat. Cell Biol. 21 (2019) 94–101, https://doi.org/10.1038/s41556-018-0249-2.

[36] Y. Chien, C. Scuoppo, X. Wang, X. Fang, B. Balgley, J.E. Bolden, P. Premsrirut, W. Luo, A. Chicas, C.S. Lee, Control of the senescence-associated secretory phenotype by NF-κB promotes senescence and enhances chemosensitivity, Gene Dev. 25 (2011) 2125–2136.

[37] Y. Ito, M. Hoare, M. Narita, Spatial and temporal control of senescence, Trends Cell Biol. 27 (2017) 820–832, https://doi.org/10.1016/j.tcb.2017.07.004.

[38] J.P. Coppe, C.K. Patil, F. Rodier, Y. Sun, D.P. Munoz, J. Goldstein, P.S. Nelson, P. Y. Desprez, J. Campisi, Senescence-associated secretory phenotypes reveal cell-nonautonomous functions of oncogenic RAS and the p53 tumor suppressor, PLoS Biol. 6 (2008) 2853–2868, https://doi.org/10.1371/journal.pbio.0060301.

[39] G. Zhou, R. Myers, Y. Li, Y. Chen, X. Shen, J. Fenyk-Melody, M. Wu, J. Ventre, T. Doebber, N. Fujii, N. Musi, M.F. Hirshman, L.J. Goodyear, D.E. Moller, Role of AMP-activated protein kinase in mechanism of metformin action, J. Clin. Investig. 108 (2001) 1167–1174, https://doi.org/10.1172/JCI13505.

[40] F. Rodier, J.P. Coppe, C.K. Patil, W.A. Hoeijmakers, D.P. Munoz, S.R. Raza, A. Freund, E. Campeau, A.R. Davalos, J. Campisi, Persistent DNA damage signalling triggers senescence-associated inflammatory cytokine secretion, Nat. Cell Biol. 11 (2009) 973–979, https://doi.org/10.1038/ncb1909.

[41] P.R. Gardner, I. Raineri, L.B. Epstein, C.W. White, Superoxide radical and iron modulate aconitase activity in mammalian cells, J. Biol. Chem. 270 (1995) 13399–13405.

[42] V. Tortora, C. Quijano, B. Freeman, R. Radi, L. Castro, Mitochondrial aconitase reaction with nitric oxide, S-nitrosoglutathione, and peroxynitrite: mechanisms and relative contributions to aconitase inactivation, Free Radical Biol. Med. 42 (2007) 1075–1088, https://doi.org/10.1016/j.freeradbiomed.2007.01.007.

[43] L. Castro, M. Rodriguez, R. Radi, Aconitase is readily inactivated by peroxynitrite, but not by its precursor, nitric oxide, J. Biol. Chem. 269 (1994) 29409–29415.

[44] S. Mansilla, V. Tórtora, F. Pignataro, S. Sastre, I. Castro, MaL. Chiribao, C. Robello, A. Zeida, J. Santos, L. Castro, Redox sensitive human mitochondrial aconitase and its interaction with frataxin: in vitro and in silico studies confirm that it takes two to tango, Free Radic. Biol. Med. 197 (2023) 71–84, https://doi.org/10.1016/j.freeradbiomed.2023.01.028.

[45] M.D. Brand, S.M. Evans, J. Mendes-Mourão, J.B. Chappell, Fluorocitrate inhibition of aconitate hydratase and the tricarboxylate carrier of rat liver mitochondria, Biochem. J. 134 (1973) 217–224, https://doi.org/10.1042/bj1340217.

[46] P. Icard, Z. Wu, L. Fournel, A. Coquerel, H. Lincet, M. Alifano, ATP citrate lyase: a central metabolic enzyme in cancer, Cancer Lett. 471 (2020) 125–134, https://doi.org/10.1016/j.canlet.2019.12.010.

[47] K.E. Wellen, G. Hatzivassiliou, U.M. Sachdeva, T.V. Bui, J.R. Cross, C.B. Thompson, ATP-citrate lyase links cellular metabolism to histone acetylation, Science 324 (2009) 1076–1080, https://doi.org/10.1126/science.1164097.

[48] D.C. Berwick, I. Hers, K.J. Heesom, S.K. Moule, J.M. Tavaréa, The identification of ATP-citrate lyase as a protein kinase B (Akt) substrate in primary adipocytes, J. Biol. Chem. 277 (2002) 33895–33900, https://doi.org/10.1074/jbc.M204681200.

[49] M.W. Pierce, J.L. Palmer, H.T. Keutmann, J. Avruch, ATP-citrate lyase. Structure of a tryptic peptide containing the phosphorylation site directed by glucagon and the cAMP-dependent protein kinase, J. Biol. Chem. 256 (1981) 8867–8870.

[50] S. Sivanand, S. Rhoades, Q. Jiang, J.V. Lee, J. Benci, J. Zhang, S. Yuan, I. Viney, S. Zhao, A. Carrer, M.J. Bennett, A.J. Minn, A.M. Weljie, R.A. Greenberg, K. E. Wellen, Nuclear acetyl-CoA production by ACLY promotes homologous recombination, Mol. Cell 67 (2017) 252–265.e6, https://doi.org/10.1016/j.molcel.2017.06.008.

[51] P. Liu, Y. Wang, X. Li, Z. Liu, Y. Sun, H. Liu, Z. Shao, E. Jiang, X. Zhou, Z. Shang, Enhanced lipid biosynthesis in oral squamous cell carcinoma cancer-associated fibroblasts contributes to tumor progression: role of IL8/AKT/p-ACLY axis, Cancer Sci. 115 (2024) 1433–1445, https://doi.org/10.1111/cas.16111.

[52] M. Dominguez, V. Truemper, A.C. Mota, B. Brüne, D. Namgaladze, Impact of ATP-citrate lyase catalytic activity and serine 455 phosphorylation on histone acetylation and inflammatory responses in human monocytic THP-1 cells, Front. Immunol. 13 (2022) 906127, https://doi.org/10.3389/fimmu.2022.906127.

[53] R.A. McCord, E. Michishita, T. Hong, E. Berber, L.D. Boxer, R. Kusumoto, S. Guan, X. Shi, O. Gozani, A.L. Burlingame, V.A. Bohr, K.F. Chua, SIRT6 stabilizes DNA-dependent Protein Kinase at chromatin for DNA double-strand break repair, Aging 1 (2009) 109–121, https://doi.org/10.18632/aging.100011.

[54] E. Michishita, R.A. McCord, E. Berber, M. Kioi, H. Padilla-Nash, M. Damian, P. Cheung, R. Kusumoto, T.L.A. Kawahara, J.C. Barrett, H.Y. Chang, V.A. Bohr, T. Ried, O. Gozani, K.F. Chua, SIRT6 is a histone H3 lysine 9 deacetylase that modulates telomeric chromatin, Nature 452 (2008) 492–496, https://doi.org/10.1038/nature06736.

[55] E. Michishita, R.A. McCord, L.D. Boxer, M.F. Barber, T. Hong, O. Gozani, K.F. Chua, Cell cycle-dependent deacetylation of telomeric histone H3 lysine K56 by human SIRT6, Cell Cycle 8 (2009) 2664–2666, https://doi.org/10.4161/cc.8.16.9367.

[56] L. Onn, M. Portillo, S. Ilic, G. Cleitman, D. Stein, S. Kaluski, I. Shirat, Z. Slobodnik, M. Einav, F. Erdel, B. Akabayov, D. Toiber, SIRT6 is a DNA double-strand break sensor, Elife 9 (2020) e51636, https://doi.org/10.7554/eLife.51636.

[57] L. Zhong, A. D'Urso, D. Toiber, C. Sebastian, R.E. Henry, D.D. Vadysirisack, A. Guimaraes, B. Marinelli, J.D. Wikstrom, T. Nir, The histone deacetylase Sirt6 regulates glucose homeostasis via Hif1α, Cell 140 (2010) 280–293.

[58] C. Sebastian, B.M. Zwaans, D.M. Silberman, M. Gymrek, A. Goren, L. Zhong, O. Ram, J. Truelove, A.R. Guimaraes, D. Toiber, C. Cosentino, J.K. Greenson, A. I. MacDonald, L. McGlynn, F. Maxwell, J. Edwards, S. Giacosa, E. Guccione, R. Weissleder, B.E. Bernstein, A. Regev, P.G. Shiels, D.B. Lombard, R. Mostoslavsky, The histone deacetylase SIRT6 is a tumor suppressor that controls cancer metabolism, Cell 151 (2012) 1185–1199, https://doi.org/10.1016/j.cell.2012.10.047.

[59] X. Cui, L. Yao, X. Yang, Y. Gao, F. Fang, J. Zhang, Q. Wang, Y. Chang, SIRT6 regulates metabolic homeostasis in skeletal muscle through activation of AMPK, Am. J. Physiol. Endocrinol. Metabol. 313 (2017) E493–E505, https://doi.org/10.1152/ajpendo.00122.2017.

[60] H.-S. Kim, C. Xiao, R.-H. Wang, T. Lahusen, X. Xu, A. Vassilopoulos, G. Vazquez-Ortiz, W.-I. Jeong, O. Park, S.H. Ki, B. Gao, C.-X. Deng, Hepatic-specific disruption of SIRT6 in mice results in fatty liver formation due to enhanced glycolysis and triglyceride synthesis, Cell Metab. 12 (2010) 224–236, https://doi.org/10.1016/j.cmet.2010.06.009.

[61] S. Kugel, R. Mostoslavsky, Chromatin and beyond: the multitasking roles for SIRT6, Trends Biochem. Sci. 39 (2014) 72–81, https://doi.org/10.1016/j.tibs.2013.12.002.

[62] M.C. Velarde, J.M. Flynn, N.U. Day, S. Melov, J. Campisi, Mitochondrial oxidative stress caused by Sod2 deficiency promotes cellular senescence and aging phenotypes in the skin, Aging (Albany NY) 4 (2012) 3–12.

[63] A. Borodkina, A. Shatrova, P. Abushik, N. Nikolsky, E. Burova, Interaction between ROS dependent DNA damage, mitochondria and p38 MAPK underlies senescence of human adult stem cells, Aging (Albany NY) 6 (2014) 481.

[64] F.R. Palma, D.R. Coelho, K. Pulakanti, M.J. Sakiyama, Y. Huang, F.T. Ogata, J. M. Danes, A. Meyer, C.M. Furdui, D.R. Spitz, A.P. Gomes, B.N. Gantner, S. Rao, V. Backman, M.G. Bonini, Histone H3.1 is a chromatin-embedded redox sensor triggered by tumor cells developing adaptive phenotypic plasticity and multidrug resistance, Cell Rep. 43 (2024) 113897, https://doi.org/10.1016/j.celrep.2024.113897.

[65] J. Martínez, I. Marmisolle, D. Tarallo, C. Quijano, Mitochondrial bioenergetics and dynamics in secretion processes, Front. Endocrinol. (2020), https://doi.org/10.3389/fendo.2020.00319.

[66] S. Herzig, R.J. Shaw, AMPK: guardian of metabolism and mitochondrial homeostasis, Nat. Rev. Mol. Cell Biol. 19 (2018) 121–135, https://doi.org/10.1038/nrm.2017.95.

[67] C. Choudhary, B.T. Weinert, Y. Nishida, E. Verdin, M. Mann, The growing landscape of lysine acetylation links metabolism and cell signalling, Nat. Rev. Mol. Cell Biol. 15 (2014) 536–550.

[68] X. Fu, S. Wan, Y.L. Lyu, L.F. Liu, H. Qi, Etoposide induces ATM-dependent mitochondrial biogenesis through AMPK activation, PLoS One 3 (2008) e2009.

[69] T. Hayakawa, M. Iwai, S. Aoki, K. Takimoto, M. Maruyama, W. Maruyama, N. Motoyama, SIRT1 suppresses the senescence-associated secretory phenotype through epigenetic gene regulation, PLoS One 10 (2015) e0116480.

[70] N. Dasgupta, R. Arnold, A. Equey, P.D. Adams, The role of the dynamic epigenetic landscape in senescence: orchestrating SASP expression, Npj Aging 10 (2024) 48, https://doi.org/10.1038/s41514-024-00172-2.

[71] S.C. Baksh, L.W.S. Finley, Metabolic coordination of cell fate by α-ketoglutarate-dependent dioxygenases, Trends Cell Biol. 31 (2021) 24–36, https://doi.org/10.1016/j.tcb.2020.09.010.

[72] J.M. Lemons, X.J. Feng, B.D. Bennett, A. Legesse-Miller, E.L. Johnson, I. Raitman, E.A. Pollina, H.A. Rabitz, J.D. Rabinowitz, H.A. Coller, Quiescent fibroblasts exhibit high metabolic activity, PLoS Biol. 8 (2010) e1000514, https://doi.org/10.1371/journal.pbio.1000514.

[73] G. Casella, R. Munk, K.M. Kim, Y. Piao, S. De, K. Abdelmohsen, M. Gorospe, Transcriptome signature of cellular senescence, Nucleic Acids Res. 47 (2019) 7294–7305, https://doi.org/10.1093/nar/gkz555.

[74] J.L. Feldman, J. Baeza, J.M. Denu, Activation of the protein deacetylase SIRT6 by long-chain fatty acids and widespread deacylation by mammalian sirtuins, J. Biol. Chem. 288 (2013) 31350–31356, https://doi.org/10.1074/jbc.C113.511261.

[75] C.C.S. Chini, H.S. Cordeiro, N.L.K. Tran, E.N. Chini, NAD metabolism: role in senescence regulation and aging, Aging Cell 23 (2024) e13920, https://doi.org/10.1111/acel.13920.

[76] S.A. Stewart, D.M. Dykxhoorn, D. Palliser, H. Mizuno, E.Y. Yu, D.S. An, D. M. Sabatini, I.S. Chen, W.C. Hahn, P.A. Sharp, R.A. Weinberg, C.D. Novina, Lentivirus-delivered stable gene silencing by RNAi in primary cells, RNA 9 (2003) 493–501.

[77] http://www.broadinstitute.org/genome_bio/trc/publicProtocols.html), (n.d.).

[78] A.R. Young, M. Narita, M. Ferreira, K. Kirschner, M. Sadaie, J.F. Darot, S. Tavare, S. Arakawa, S. Shimizu, F.M. Watt, M. Narita, Autophagy mediates the mitotic senescence transition, Gene Dev. 23 (2009) 798–803, https://doi.org/10.1101/gad.519709.

[79] R.I. Martínez-Zamudio, A. Stefa, J.A. Nabuco Leva Ferreira Freitas, T. Vasilopoulos, M. Simpson, G. Doré, P.-F. Roux, M.A. Galan, R.J. Chokshi, O. Bischof, U. Herbig, Escape from oncogene-induced senescence is controlled by POU2F2 and memorized by chromatin scars, Cell Genomics 3 (2023) 100293, https://doi.org/10.1016/j.xgen.2023.100293.

[80] X. Han, H. Tai, X. Wang, Z. Wang, J. Zhou, X. Wei, Y. Ding, H. Gong, C. Mo, J. Zhang, J. Qin, Y. Ma, N. Huang, R. Xiang, H. Xiao, AMPK activation protects cells from oxidative stress-induced senescence via autophagic flux restoration and intracellular NAD$^+$ elevation, Aging Cell 15 (2016) 416–427, https://doi.org/10.1111/acel.12446.

[81] K.J. Livak, T.D. Schmittgen, Analysis of relative gene expression data using real-time quantitative PCR and the 2(-Delta Delta C(T)) Method, Methods 25 (2001) 402–408, https://doi.org/10.1006/meth.2001.1262.

[82] I. Dimauro, T. Pearson, D. Caporossi, M.J. Jackson, A simple protocol for the subcellular fractionation of skeletal muscle cells and tissue, BMC Res. Notes 5 (2012) 513, https://doi.org/10.1186/1756-0500-5-513.

[83] L.A. Castro, R.L. Robalinho, A. Cayota, R. Meneghini, R. Radi, Nitric oxide and peroxynitrite-dependent aconitase inactivation and iron-regulatory protein-1 activation in mammalian fibroblasts, Arch. Biochem. Biophys. 359 (1998) 215–224, https://doi.org/10.1006/abbi.1998.0898.

[84] P. Irigoyen, S. Mansilla, L. Castro, A. Cassina, R. Sapiro, Mitochondrial function and reactive oxygen species production during human sperm capacitation: unraveling key players, FASEB J. 38 (2024) e23486, https://doi.org/10.1096/fj.202301957RR.

[85] W. Gardner, R.C.W. P, Application of the aconitase method to the assay of superoxide in the mitochondrial matrices of cultured cells: effects of oxygen, redox cycling agent, TNF-α, IL-1, LPS and inhibitors of respiration, in: K.J.A. Davies, F. Ursini (Eds.), The Oxygen Paradox, Cleup University Press., Padova, 1995, pp. 33–50.

[86] J. Liu, L. Cao, J. Chen, S. Song, I.H. Lee, C. Quijano, H. Liu, K. Keyvanfar, H. Chen, L.Y. Cao, B.H. Ahn, N.G. Kumar, I. Rovira, X.L. Xu, M. van Lohuizen, N. Motoyama, C.X. Deng, T. Finkel, Bmi1 regulates mitochondrial function and the DNA damage response pathway, Nature 459 (2009) 387–392, https://doi.org/10.1038/nature08040.

[87] B. Kalyanaraman, V. Darley-Usmar, K.J.A. Davies, P.A. Dennery, H.J. Forman, M. B. Grisham, G.E. Mann, K. Moore, L.J. Roberts, H. Ischiropoulos, Measuring reactive oxygen and nitrogen species with fluorescent probes: challenges and limitations, Free Radic. Biol. Med. 52 (2012) 1–6, https://doi.org/10.1016/j.freeradbiomed.2011.09.030.